

9.5k words; Figure 10; Table 5; 127 refs; Updated: 4 June 2005)

Book: Oxide Nanomaterials, John Wiley & Sons, in press.

Chapter 1 Theory of size, confinement, and oxidation effects

Chang Q. Sun*

*School of Electrical and Electronic Engineering, Nanyang Technological University, Singapore
639798 and Institute of Advanced Materials Physics and Faculty of Science, Tianjin University,
300072, P. R. China*

Chapter 1	<i>Theory of size, confinement, and oxidation effects</i>	1
1	<i>Introduction</i>	2
2	<i>Effects of size and confinement</i>	5
2.1	<i>Basic concepts</i>	5
2.1.1	<i>Intraatomic trapping of an isolated atom</i>	5
2.1.2	<i>Interatomic bonding and intercluster coupling</i>	5
2.1.3	<i>Hamiltonian and energy band</i>	6
2.1.4	<i>Atomic cohesive energy and thermal stability</i>	7
2.2	<i>Surface boundary effect</i>	8
2.2.1	<i>Barrier confinement vs. quantum uncertainty</i>	8
2.2.2	<i>Atomic CN reduction</i>	9
2.3	<i>Surface-to-volume ratio</i>	9
2.4	<i>Bond order-length-strength (BOLS) correlation</i>	10
2.4.1	<i>Bond order-length correlation</i>	10
2.4.2	<i>Bond length-strength correlation</i>	11
2.4.3	<i>Densification of mass, charge, and energy</i>	13
2.5	<i>Shape-and-size dependency</i>	13
2.5.1	<i>Scaling relation</i>	13
2.5.2	<i>Cohesive energy modification</i>	14
2.5.3	<i>Hamiltonian perturbation</i>	15
2.5.4	<i>Electron-phonon coupling</i>	16
2.5.5	<i>Mechanical strength</i>	17
2.6	<i>Summary</i>	18
3	<i>Effect of oxidation</i>	21
3.1	<i>Bond-band-barrier (BBB) correlation</i>	21
3.2	<i>Experimental evidence</i>	22
3.2.1	<i>Surface potential barrier and bond geometry</i>	22
3.2.2	<i>Valence density of states</i>	23
3.2.3	<i>Lone pair interaction</i>	24
3.2.4	<i>Bond forming kinetics</i>	25
3.3	<i>Summary</i>	25
4	<i>Conclusion</i>	26
	<i>References</i>	36

* E-mail: ecqsun@ntu.edu.sg; URL: www.ntu.edu.sg/home/ecqsun/

I Introduction

Both oxidation and size reduction form the essential entities that dictate the behaviour of a nanostructured oxide. The atomic and electronic processes of oxidation destroy the initially metallic bond to create new kinds of bonds that determine the behavior of the oxides to vary from their parent metals.¹ Oxygen interaction with atoms of metals relates to the technical processes of corrosion, bulk oxidation, and heterogeneous catalysis, etc.² Studies of these processes laid the foundations for applications in microelectronics (gate devices and deep submicron integrated circuit technologies), photo-electronics (photoluminescence, photo-conductance and field emission), magneto-electronics (superconductivity and colossal magneto-resistance) and dielectrics (ferro-, piezo-, pyro-electrics).³ Involvement of interatomic interaction causes the performance of a solid, or a cluster of atoms, to vary from that of an isolated atom. Adjustment of the relative number of the lower-coordinated surface atoms forms an additional freedom that allows one to tune the properties of a nanosolid with respect to that of its bulk counterpart. Properties of nanosolids determined by their shapes and sizes are indeed fascinating, which form the basis of the emerging field of nanoscience and nanotechnology that has been recognized as the key significance in science, technology, and economics in the 21st century.

How do the interatomic bonding and the surface atomic portion govern the behavior of a nanosolid? What is the consequence of oxidation? How to make use of the joint effect of size reduction and oxidation in predictable design of oxide nanomaterials?

The size induced property change of nanostructures has inspired tremendous theoretical interest. For instance, a number of models have been developed to explain how the size reduction could induce the blue shift in the photoluminescence (PL) of nanosemiconductors. An *impurity luminescent center* model⁴ assumed that the PL blue shift arise from different types of impurity centers in the solid and suggested that the density and types of the impurity centers vary with particle size. *Surface states and surface alloying* mechanism^{5,6} proposed that the PL blue shift originate from the extent of surface passivation that is subject to the processing parameters, aging conditions, and operation temperatures.⁷ The model of *Inter-cluster interaction and oxidation*⁸ also claimed the responsibility for the PL blue shift. The most elegant model for the PL blue shift could be the “quantum confinement (QC)” theory.^{9,10,11,12,13} According to the QC theory, the PL energy corresponds to the band gap expansion dictated by electron-hole (e-h) pair (or exciton) production:

$$E_G(R) - E_G(\infty) = \pi^2 \hbar^2 / (2\mu R^2) - 1.786e^2 / (\epsilon_r R) + 0.284E_R \quad (1)$$

where $\mu = m_h^* m_e^* / (m_h^* + m_e^*)$, being the reduced mass of the e-h pair, is an adjustable parameter. The E_G expansion originates from the addition of the kinetic energy, E_K , and the Coulomb interaction, E_p , of the e-h pairs that are separated by a distance of the particle radius, R , and contribution of the Rydberg or spatial correlation (electron-electron interaction) energy E_R for the bulk semiconductor. The effective dielectric constant ϵ_r and the effective mass, μ , describe the effect of the homogeneous medium in the quantum box, which is simplified as a mono-trapping central potential by extending the dimension of a single atom, d_0 , to that of the solid, D . According to the QC theory, electrons in the conduction band and holes in the valence band are confined spatially by the potential barrier of the surface, or trapped by the potential well of the quantum box. Because of the confinement of both the electrons and the holes, the lowest energy optical transition from the valence to the conduction band increases in energy, effectively increasing the E_G . The sum of the kinetic and potential energy of the freely moving carriers is responsible for the E_G expansion, and therefore, the width of the confined E_G grows as the characteristic dimensions of the crystallites decrease.

In contrast, a free-exciton collision model¹⁴ suggested that the E_G expansion arises from the contribution of thermally activated phonons in the grain boundaries rather than the QC effect. During PL measurement, the excitation laser heats the free excitons that then collide with the boundaries of the nanometer-sized fragments. The laser heating the free-excitons up to the temperature in excess of the activation energy required for the self-trapping gives rise to the extremely hot self-trapping excitons (STE's). Because the resulting temperature of the STE's is much higher than the lattice temperature, the cooling of the STE's is dominated by the emission of phonons. However, if the STE temperature comes into equilibrium with the lattice temperature, the absorption of lattice phonons becomes possible. As a result, the blue shift of the STE-PL band is suggested to originate from the activation of hot-phonon-assisted electronic transitions. The blue shift of the STE-PL band depends on the temperature of laser-heated free-excitons that in turn is determined by the size of nano-fragments. This event happens because the temperature (kinetic energy) of the laser-heated free-exciton increases with the number of boundary collisions, which tends to be higher with decreasing size of the nano-fragments. The energy gained from laser heating of the exciton increases with decreasing nanosolid size in an $\exp(1/R)$ way.

Another typical issue of nanostructures is their thermal stability. The melting point (T_m) of an isolated nanosolid, or a system with weakly linked nanoparticles, drops with solid size (called as supercooling), while the T_m may rise (called as superheating) for an embedded nano-system due to the interfacial effect. The T_m is characterized by the Lindermann's criterion¹⁵ of atomic vibration abruption or Born's criterion¹⁶ of shear modulus disappearance at the T_m . The T_m elevation or suppression or the mode of melting in the nanometer regime have been described with the following models: (i)

homogeneous melting and growth;^{17,18} (ii) random fluctuation melting;¹⁹ (ii) liquid shell nucleation and growth;^{20,21,22,23} (iii) liquid-drop²⁴ formation; (iv) lattice-vibrational instability^{25,26} and; (v) surface-phonon instability.^{27,28}

The challenge is how to correlate these outstanding mechanisms to the effect of bond order loss of the lower-coordinated surface atoms or the effect of confinement. The origin for one single phenomenon must be intrinsically common to others caused by the same origin of size reduction. Understanding the mechanisms for both size reduction and oxidation and their joint contribution is critical to understanding the behavior of nanostructured oxide materials and related devices.

This chapter describes a bond order-length-strength (BOLS) correlation mechanism²⁹ for the effect of physical size (bond order loss) and a chemical-bond -- valence-band -- potential-barrier (BBB) correlation mechanism¹ for the effect of oxidation (bond nature alteration) on the performance of a nanostructured oxide. The BBB correlation indicates the essentiality of sp-orbital hybridization of an oxygen atom upon reacting with atoms in solid phase. In the process of oxidation, electronic holes, non-bonding lone pairs, lone-pair induced anti-bonding dipoles, and hydrogen bond like are involved through charge transportation and polarization, which dictate the performance of an oxide. Charge transport from metal to oxygen creates the band gap, which turns the metal to be a semiconductor or an insulator; lone pair induced charge polarization lowers the work function of the surface while hydrogen bond like formation due to overdosing with the oxygen additives restores the work function. The often-overlooked events of nonbonding and antibonding are expected to play significant roles in the functioning of an oxide.

The BOLS correlation mechanism indicates the significance of bond order loss of an atom at site surrounding a defect or near the edge of a surface or in an amorphous phase in which the coordination (CN) reduction (deviation of bond order, length, and angle) distributes randomly. Bond order loss causes the remaining bonds of the lower-coordinated atom to contract spontaneously associated with bond-strength gain or atomic potential well depression, which localize electrons and enhance the density of charge, mass, and energy in the relaxed region. The energy density rise in the relaxed region perturbs the Hamiltonian and the associated properties such as the band-gap width, core-level energy, Stokes shift (electron-phonon interaction), and dielectric susceptibility. On the other hand, bond-order loss lowers the cohesive energy of the lower-coordinated atom, which dictates the thermodynamic process such as self-assembly growth, atomic vibration, thermal stability, and activation energies for atomic dislocation, diffusion and chemical reaction.

Consistent insight and numerical agreement with observations evidence the impact of bond nature alteration in oxidation and bond order loss in size reduction and the essentiality and validity of the corresponding BBB and BOLS correlation mechanisms in describing oxide nanomaterials.

2 Effects of size and confinement

2.1 Basic concepts

2.1.1 Intraatomic trapping

Electrons of a single atom confined by the intra-atomic trapping potential, $V_{atom}(r)$, move around the central ion core in a standing-wave form inside the potential well. The $V_{atom}(r)$ takes a value that varies from several eV to infinity, depending on the orbitals in which electrons are revolving. The Hamiltonian and the corresponding eigen wave functions and the eigen energies for an electron in the isolated atom are given as:

$$\hat{H}_0 = -\frac{\hbar^2 \nabla^2}{2m} + V_{atom}(r)$$

$$\phi_v(r) \propto \sin^2(k_n r), \text{ and}$$

$$E(n) = \hbar^2 k_n^2 / 2m_e; k_n = 2n\pi/d_0^2, n = 1, 2, 3, \dots$$

the atomic diameter d_0 corresponds to the dimension of the potential well of the atom. The branch numbers (n) correspond to different energy levels. The energy separation between the nearest two levels depends on $(n+1)^2 - n^2 = 2n+1$.

2.1.2 Interatomic bonding and intercluster coupling

When two atoms or more joined as a whole, interatomic interaction comes into play, which causes the performance of a cluster of atoms from that of an isolated atom. The interatomic bonding is essential to make a solid or even a liquid. Considering an assembly composed of n particles of mean size K_j and with each particle, there are N_j atoms, the total binding energy, $V_{cry}(r, n, N_j)$, is:³⁰

$$\begin{aligned} V_{cry}(r, n, N_j) &= \sum_n \sum_{l \neq i} \sum_i v(r_{li}) \\ &= \frac{n}{2} \left[N_j \sum_{i=1} v(r_{li}) + \sum_{k \neq j} V(K_{kj}) \right] \\ &\cong \frac{n}{2} \left[N_j^2 v(d_0) + nV(K_j) \right] \end{aligned} \tag{2}$$

The $V_{cry}(r, n, N_j)$ sums over all the N_j atoms and the n particles. The high order r_{li} is a certain fold of the nearest atomic spacing, d_0 . Interaction between the nearest clusters, k and j , $V(K_{kj})$, is negligible if

the K_{kj} is considerably large. Normally, the intercluster interaction, $V(K_{kj})$, is much weaker than the interatomic interaction, if the cluster is treated as an electric or a magnetic dipole of which the Van der Waals or the super-paramagnetic potentials dominate.

2.1.3 Hamiltonian and energy band

According to the band theory, the Hamiltonian for an electron inside a solid is in the form:

$$\hat{H} = \hat{H}_0 + \hat{H}' = -\frac{\hbar^2 \nabla^2}{2m} + V_{atom}(r) + V_{cry}(r + R_C) \quad (3)$$

where the $\hat{H}' = V_{cry}(r) = V_{cry}(r + R_C)$ is the periodic potential of the crystal. R_C is the lattice constant. According to the nearly-free-electron approximation, the E_G between the valence and the conduction bands originates from the crystal potential. The width of the gap depends on the integral of the crystal potential in combination with the Bloch wave of the nearly free electron, $\phi(k_i, r)$:

$$E_G = 2|V_1(k_l)|, \text{ and } V_1(k_l) = \langle \phi(k_l, r) | V(r + R_C) | \phi(k_l, r) \rangle \quad (4)$$

where k_l is the wave-vector and $k_l = 2l\pi/R_C$. Actually, the E_G is simply twice the first Fourier coefficient of the crystal potential.

As illustrated in Figure 1, the energy levels of an isolated atom will evolve into energy bands when interatomic bonding is involved. When a system contains two atoms, such as a dimer like H_2 molecules, the single energy level splits into two sublevels. The presence of interatomic interaction lowers the center of the two sublevels, which is termed as core level shift. Increasing the number of atoms up to N_j , the single energy level will expand into a band within which there are N_j sublevels.

What distinguishes a nanosolid from a bulk chunk is that for the former the N_j is accountable, while for the latter the N_j is too large to be accounted despite the portion of the lower-coordinated atoms in the surface skin. Therefore, the classical band theories are valid for a solid that may contain any number of atoms. As detected with x-ray photoelectron spectroscopy (XPS), the density-of-states (DOS) of a core band for a nanosolid exhibits band-like features rather than the discrete spectral lines of a single atom. If the N_j is sufficiently small, the separation between the sublevels is resolvable. The energy level spacing between the successive sublevels in the valence band, known as the Kubo gap ($\delta_K = 4E_F/3N_j$), decreases with increasing the number of valence electrons of the system, N_j .³¹ Where E_F is the Fermi energy of the bulk. Because of the presence of the δ_K in an individual nanosolid, properties such as electron conductivity and magnetic susceptibility exhibit quantized features.³²

Figure 1 The involvement of interatomic interaction evolves a single energy level to the energy band when a particle grows from a single atom to a bulk solid that contains N_j atoms. Indicated are the work function ϕ , band gap E_G , core level shift ΔE_v , bandwidth E_B . The number of allowed sublevels in a certain band equals the number of atoms of the solid.³³

According to the tight-binding approximation, the energy dispersion of an electron in the v th core band follows the relation:

$$\begin{aligned} E_v(k) &= E_v(1) + \Delta E_v(\infty) + \Delta E_B(k_l, R_C, z) \\ &= E_v(1) - (\beta + 2\alpha) + 4\alpha\Omega(k_l, R_C, z) \end{aligned} \quad (5)$$

where,

$E_v(1) = \langle \phi_v(r) | \hat{H}_0 | \phi_v(r) \rangle$ is the v th energy level of an isolated atom.

$\beta = -\langle \phi_v(r) | V_{cry}(r) | \phi_v(r) \rangle$ is the crystal potential effect on the specific core electron at site r .

$\alpha = -\langle \phi_v(r - R_C) | V_{cry}(r - R_C) | \phi_v(r - R_C) \rangle$ is the crystal potential effect on the coordinate neighbouring electrons. For an fcc structure example, the structure factor, $\Omega(k_l, R_C) = \sum_z \sin^2(k_l R_C / 2)$. The sum is over all the contributing coordinates (z) surrounding the specific atom in the solid.

Eqs (4) and (5) indicate that the E_G , the energy shift $\Delta E_v(\infty) = -(\beta + 2\alpha)$ of the $E_v(1)$ and the bandwidth ΔE_B (last term in Eq (5)) are all functions of the crystal potential. Any perturbation to the crystal potential will vary these quantities accordingly as the change of the Bloch wavefunction is negligible in the first order approximation. The band structure has nothing to do with the actual occupancy of the particular orbitals or events such as electron-hole pair creation or recombination, or the processes of PL and PA that involve electron-phonon coupling effect. Without the crystal potential, neither the E_G expansion nor the core-level shift would be possible; without the inter-atomic binding, neither a solid nor even a liquid would form.

If one intends to modify the properties of a solid, one has to find ways of modulating the crystal potential physically or chemically. Bond nature alteration by chemical reaction or bond length relaxation by size reduction, as discussed in the following sections, will be the effective ways of modulating the interatomic potential.

2.1.4 Atomic cohesive energy and thermal stability

Another key concept is the cohesive energy per discrete atom. The binding energy density per unit volume contributes to the Hamiltonian that determines the entire band structure and related properties, while the atomic cohesive energy determines the activation energy for thermally and mechanically activated processes including self assembly growth, phase transition, solid-liquid transition, evaporation, atomic dislocation, diffusion and chemical reaction.

The cohesive energy (E_{coh}) of a solid containing N_j atoms equals to the energy dividing the crystal into individually isolated atoms by breaking all the bonds of the solid. If no atomic CN reduction is considered, the E_{coh} is the sum of bond energy over all the z_b coordinates of all the N_j atoms:

$$E_{\text{coh}}(N_j) = \sum_{N_j} \sum_{z_i} E_i \cong N_j z_b E_b = N_j E_B \quad (6)$$

The cohesive energy for a single atom, E_B , is the sum of the single bond energy E_b over the atomic CN, $E_B = z_b E_b$. One may consider a thermally activated process such as phase transition in which all the bonds are loosened to a certain extent due to thermal activation. The energy required for such a process is a certain portion of the atomic E_B though the exact portion may change from process to process. If one considers the relative change to the bulk value, the portion will not be accounted. This approximation is convenient in practice, as one should be concerned with the origins and the trends of changes. Therefore, bulk properties such as thermal stability of a solid could be related directly to the atomic cohesive energy – the product of the bond number and bond energy of the specific atom.

2.2 Boundary conditions

2.2.1 Barrier confinement vs. quantum uncertainty

The termination of lattice periodicity in the surface normal direction has two effects. One is the creation of the surface potential barrier (SPB), or work function, or contact potential, and the other is the reduction of the atomic CN. The SPB is the intrinsic feature of a surface, which confines only electrons that are freely moving inside the solid. However, the SPB has nothing to do with the *strongly localized* electrons in deeper core bands or with those forming electron pairs in a bond. The localized electrons do not suffer such barrier confinement at all as the localization length is far shorter than the particle size.

According to the quantum uncertainty principle, reducing the dimension (D) of the space inside which energetic particles are moving increases the fluctuation, rather than the average value, of the momentum, p , or kinetic energy, E_k , of the moving particles:

$$\begin{aligned}
\Delta p D &\geq \hbar/2 \\
p &= \bar{p} \pm \Delta p \\
\overline{E_k} &= \overline{p^2} / (2\mu)
\end{aligned}
\tag{7}$$

where \hbar being the Plank constant corresponds to the minimal quanta in energy and momentum spaces and μ is the mass of the moving particle. The kinetic energy of a freely moving particle is increased by a negligible amount due to the confinement effect that follows the quantum uncertainty principle. If the average momentum $\bar{p} = 0$, then $\Delta p \cong p$, the kinetic energy enhancement would be: $\overline{E_k} = \Delta p^2 / (2\mu) = (\hbar/2D)^2 / 2\mu \approx D^{-2} 10^{-18} (eV)$. If the D is taken as 10 nm, the E_k is increased by 10^{-2} eV. Therefore, the SPB confinement causes energy-rise of neither the freely moving carriers nor the localized ones.

2.2.2 Atomic CN reduction

The atomic CN reduction is referred to the standard value of 12 in the bulk of an fcc structure irrespective of the bond nature or the crystal structure. Atomic CN reduction is referred to an atom with coordinate less than the standard value of 12. The CN is 2 for an atom in the interior of a monatomic chain or an atom at the open end of a single-walled carbon nanotube (CNT); while in the CNT wall, the CN is 3. For an atom in the fcc unit cell, the CN varies from site to site. The CN of an atom at the edge or corner differs from the CN of an atom in the plane or the central of the unit cell. Atoms with deformed bond lengths or deviated angles in the CNT are the same as those in amorphous states that are characterised with the band tail states.³⁴ For example, the effective CN of an atom in diamond tetrahedron is the same as that in an fcc structure as a tetrahedron unit cell is an interlock of two fcc unit cells. The CN of an atom in a highly curved surface is even lower compared with the CN of an atom at a flat surface. For a negatively curved surface (such as the inner side of a pore or a bubble), the CN may be slightly higher than that of an atom at the flat surface. Therefore, from the atomic CN reduction point of view, there is no substantial difference in nature between a nanosolid, a nanopore, and a flat surface. This premise can be extended to the structural defects or defaults such as voids surrounding which atoms are suffer from CN reduction. Unlike a nansolid with ordered CN reduction at the surface, an amorphous solid possesses defects that are distributed randomly.

2.3 Surface-to-volume ratio

It is easy to derive the volume or number ratio of a certain atomic layer, denoted i , to that of the entire solid by differentiating the natural logarithm of the volume,

$$\gamma_{ij} = \frac{N_i}{N_j} = \frac{V_i}{V_j} = dLn(V_j) = \frac{\tau dR_j}{R_j} = \frac{\tau c_i}{K_j} \quad (8)$$

where $K_j = R_j/d_0$ is the dimensionless form of size, which is the number of atoms lined along the radius of a spherical dot ($\tau = 3$), a rod ($\tau = 2$), or cross the thickness of a thin plate ($\tau = 1$). The volume of a solid is proportional to R_j^τ . For a hollow system, the γ_{ij} should count both external and internal sides of the hollow structure.

With reducing particle size, performance of surface atoms become dominant because at the lower end of size limit ($K_j \rightarrow \tau c_i$) γ_1 approaches unity. At $K_j = 1$, the solid will degenerate into an isolated atom. Therefore, the γ_{ij} covers the whole range of sizes and various shapes. The definition of dimensionality (τ) herein differs from the convention in transport or quantum confinement considerations in which a nano-sphere is zero-dimension (quantum dot), a rod as one dimension (quantum wire), and a plate two dimension (quantum well). If we count atom by atom, the number ratio and the property change will show quantized oscillation features at smaller sizes, which varies from structure to structure.³⁵

2.4 Bond order-length-strength (BOLS) correlation

2.4.1 Bond order-length correlation

As the consequence of bond order loss, the remaining bonds of the lower-coordinated atoms contract spontaneously. As ascerted by Goldschmidt³⁶ and Pauling,³⁷ the ionic and the metallic radius of the atom would shrink spontaneously if the CN of an atom is reduced. The CN reduction induced bond contraction is independent of the nature of the specific bond or structural phases.³⁸ A 10% contraction of spacing between the first and second atomic surface layers has been detected in the liquid phase of Sn, Hg, Ga, and In.³⁹ As impurity has induced 8% bond contraction around the impurity (acceptor dopant As) at the Te sublattice in CdTe has also been observed using EXAFS (extended X-ray absorption fine structure) and XANES (X-ray absorption near edge spectroscopy).⁴⁰ Therefore, CN reduction induced bond contraction is common.

Figure 2a illustrates the CN dependence of bond length. The solid curve, $c_i(z_i)$, formulates the Goldschmidt premise which states that an ionic radius contracts by 12%, 4%, and 3%, if the CN of the atom reduces from 12 to 4, 6 and 8, respectively. Feibelman⁴¹ has noted a 30% contraction of the dimer bond of Ti and Zr, and a 40% contraction of the dimer-bond of Vanadium, which is also in line with the formulation.

Figure 2 ([link](#)) illustration of the BOLS correlation. Solid curve in (a) is the contraction coefficient c_i derived from the notations of Goldschmidt³⁶ (open circles) and Feibelman⁴¹ (open square). As a spontaneous process of bond contraction, the bond energy at equilibrium atomic separation will rise in absolute energy, $E_i = c_i^{-m}E_b$. The m is a parameter that represents the nature of the bond. However, the atomic cohesive energy, z_iE_i , changes with both the m and z_i values. (b) Atomic CN reduction modified pairing potential energy. CN reduction causes the bond to contract from one unit (in d_0) to c_i and the cohesive energy per coordinate increases from one unit to c_i^{-m} unit. Separation between $E_i(T)$ and $E_i(0)$ is the thermal vibration energy. Separation between $E_i(T_{m,i})$ and $E_i(T)$ corresponds to melting energy per bond at T , which dominates the mechanical strength. $T_{m,i}$ is the melting point. η_{2i} is $1/z_i$ fold energy atomizing an atom in molten state.

2.4.2 Bond length-strength correlation

As a consequence of the spontaneous process of bond contraction, the bond strength will gain, towards a lowering of the system energy. The contraction coefficient and the associated bond energy gain form the subject of the BOLS correlation mechanism that is formulated as:

$$\begin{cases} c_i(z_i) = d_i/d_0 = 2/\{1 + \exp[(12 - z_i)/(8z_i)]\} & (BOLS - coefficient) \\ E_i = c_i^{-m}E_b & (Single - bond - energy) \\ E_{B,i} = z_iE_i & (atomic - cohesive - energy) \end{cases} \quad (9)$$

Subscript i denotes an atom in the i th atomic layer, which is countered up to three from the outermost atomic layer to the center of the solid as no CN-reduction is expected for $i > 3$. The index m is a key indicator for the nature of the bond. Experience⁴² revealed that for Au, Ag, Ni metals, $m \equiv 1$; for alloys and compounds, m is around four; for C and Si, the m has been optimized to be 2.56⁴³ and 4.88,⁴⁴ respectively. The m value may vary if the bond nature evolves with atomic CN.⁴⁵ If the surface bond expands in cases, we simply expand the c_i from a value that is smaller than unity to greater, and the m value from positive to negative to represent the spontaneous process of which the system energy is minimized. The $c_i(z_i)$ depends on the effective CN rather than a certain order of CN. The z_i also varies with the particle size due to the change of the surface curvature. The z_i takes the following values:⁴⁴

$$z_1 = \begin{cases} 4(1 - 0.75/K_j) & \text{curved - surface} \\ 4 & \text{flat - surface} \end{cases} \quad (10)$$

Generally, $z_2 = 6$ and $z_3 = 8$ or 12 .

Figure 2b illustrates schematically the BOLS correlation using a simple interatomic pairing potential, $u(r)$. When the CN of an atom is reduced, the equilibrium atomic distance will contract from one unit (in d_0) to c_i and the cohesive energy of the shortened bond will increase in magnitude from one unit (in E_b) to c_i^{-m} . The solid and the broken $u(r)$ curves correspond to the pairing potential with and without CN reduction. The BOLS correlation has nothing to do with the particular form of the pairing potential as the approach involves only atomic distance at equilibrium. The bond length-strength correlation herein is consistent with the trend reported by Bahn and Jacobsen⁴⁶ though the extents of bond contraction and energy enhancement therein vary from situation to situation.

There are several characteristic energies in Figure 2b, which correspond to the following facts:

- (i) $T_{m,i}$ being the local melting point is proportional to the cohesive energy, $z_i E_i(0)$,⁴⁷ per atom with z_i coordinate.⁴⁸
- (ii) Separation between $E = 0$ and $E_i(T)$, or $\eta_{1i}(T_{m,i} - T) + \eta_{2i}$, corresponds to the cohesive energy per coordinate, E_i , at T , being energy required for bond fracture under mechanical or thermal stimulus. η_{1i} is the specific heat per coordinate.
- (iii) The separation between $E = 0$ and $E_i(T_m)$, or η_{2i} , is the $1/z_i$ fold energy that is required for atomization of an atom in molten state.
- (iv) The spacing between $E_i(T)$ and $E_i(0)$ is the vibration energy purely due to thermal excitation.
- (v) The energy contributing to mechanical strength is the separation between the $E_i(T_m)$ and the $E_i(T)$, as a molten phase is extremely soft and highly compressible.⁴⁹

Values of η_{1i} and η_{2i} can be obtained with the known c_i^{-m} and the bulk η_{1b} and η_{2b} values that vary only with crystal structures as given in Table 1.

Table 1 Relation between the bond energy E_b and the T_m of various structures.²⁴ $\eta_{2b} < 0$ for an fcc structure means that the energy required for breaking all the bonds of an atom in molten state is included in the term of $\eta_{1b}zT_m$ and therefore the η_{2b} exaggerates the specific heat per CN.

$E_b = \eta_{1b}T_m + \eta_{2b}$	fcc	bcc	Diamond structure
----------------------------------	-----	-----	-------------------

$\eta_{1b} (10^{-4} \text{ eV/K})$	5.542	5.919	5.736
$\eta_{2b} (\text{eV})$	-0.24	0.0364	1.29

2.4.3 Densification of mass, charge, and energy

Figure 3 compares the potential well in the QC convention with that of the BOLS for a nanosolid. The QC convention extends the monotrapping potential of an isolated atom by expanding the size from d_0 to D . BOLS scheme covers contribution from individual atoms that are described with multi-trapping-centre potential wells, and the effect of atomic CN reduction in the surface skin. Atomic CN reduction induced bond-strength gain depresses the potential well of trapping in the surface skin. Therefore, the density of charge, energy, and mass in the relaxed surface region are higher than other sites inside the solid. Consequently, surface stress that is in the dimension of energy density will increase in the relaxed region. Electrons in the relaxed region are more localized because of the depression of the potential well of trapping, which lowers the work function and conductivity in the surface region, but enhances the angular momentum of the surface atoms.³⁵

Figure 3 ([link](#)) Schematic illustration of conventional quantum well (upper part) with a monotrapping center extended from that of a single atom, and the BOLS derived nanosolid potential (lower part) with multi-trap centers and CN reduction induced features. In the relaxed surface region, the density of charge, energy and mass will be higher than other sites due to atomic CN reduction.

2.5 Shape-and-size dependency

2.5.1 Scaling relation

Generally, the mean relative change of a measurable quantity of a nanosolid containing N_j atoms, with dimension K_j , can be expressed as $Q(K_j)$; and as $Q(\infty)$ for the same solid without contribution from bond order loss. The correlation between the $Q(K_j)$ and $Q(\infty) = N_j q_0$ and the relative change of Q due to bond order loss is given as:

$$\begin{aligned}
Q(K_j) &= N_j q_0 + N_s (q_s - q_0) \\
\frac{\Delta Q(K_j)}{Q(\infty)} &= \frac{Q(K_j) - Q(\infty)}{Q(\infty)} = \frac{N_s}{N_j} \left(\frac{q_s}{q_0} - 1 \right) \\
&= \sum_{i \leq 3} \gamma_{ij} (\Delta q_i / q_0) = \Delta_{qj}
\end{aligned} \tag{11}$$

The weighting factor, γ_{ij} , represents the geometrical contributions from dimension (K_j) and dimensionality (τ) of the solid, which determines the magnitude of change. The quantity $\Delta q_i/q_0$ is the origin of change. The $\sum_{i \leq 3} \gamma_{ij}$ drops in a K_j^{-1} fashion from unity to infinitely small when the solid grows from atomic level to infinitely large. For a spherical dot at the lower end of the size limit, $K_j = 1.5$ ($K_j d_0 = 0.43$ nm for an Au spherical dot example), $z_1 = 2$, $\gamma_{1j} = 1$, and $\gamma_{2j} = \gamma_{3j} = 0$, which is identical in situation to an atom in a monatomic chain (MC) despite the orientation of the two interatomic bonds. Actually, the bond orientation is not involved in the modeling iteration. Therefore, the performance of an atom in the smallest nanosolid is a mimic of an atom in an MC of the same element without presence of external stimulus such as stretching or heating. At the lower end of the size limit, the property change of a nanosolid relates directly to the behavior of a single bond.

Generally, experimentally observed size-and-shape dependence of a detectable quantity follows a scaling relation. Equilibrating the scaling relation to Eq (9), one has:

$$Q(K_j) - Q(\infty) = \begin{cases} bK_j^{-1} & (\text{measurement}) \\ Q(\infty) \times \Delta_{qj} & (\text{theory}) \end{cases} \quad (12)$$

where the slope $b \equiv Q(\infty) \times \Delta_{qj} \times K_j \cong \text{constant}$ is the focus of various modeling pursuits. The $\Delta_j \propto K_j^{-1}$ varies simply with the $\gamma_{ij}(\tau, K_j, c_i)$ if the functional dependence of $q(z_i, c_i, m)$ on the atomic CN, bond length, and bond energy is given.

2.5.2 Cohesive energy modification

The heat energy required for loosening an atom is a certain portion of the atomic E_B that varies with not only the atomic CN but also the bond strength. The variation of the mean E_B with size is responsible for the fall (supercooling) or rise (superheating) of the T_C (critical temperature for melting, phase transition, or evaporation) of a surface and a nanosolid. The E_B is also responsible for other thermally activated behaviors such as phase transition, catalytic reactivity, crystal structural stability, alloy formation (segregation and diffusion), and stability of electrically charged particles (Coulomb explosion). The cohesive energy also determines crystal growth and atomic diffusion, and atomic gliding displacement that determine the ductility of nanosolids.

The BOLS correlation considers contribution from atoms in the shells of the surface skin. Using the spherical dot containing N_j atoms, the average $\langle E_{\text{coh}}(N_j) \rangle$, or $\langle E_B(N_j) \rangle$ is,

$$\begin{aligned}
\langle E_{coh}(N_j) \rangle &= N_j z_b E_b + \sum_{i \leq 3} N_i (z_i E_i - z_b E_b) \\
&= N_j E_B(\infty) + \sum_{i \leq 3} N_i z_b E_b (z_{ib} E_{ib} - 1) \\
&= E_{coh}(\infty) \left[1 + \sum_{i \leq 3} \gamma_{ij} (z_{ib} c_i^{-m} - 1) \right] = E_{coh}(\infty) (1 + \Delta_B)
\end{aligned}$$

or, $\Delta E_B(K_j)/E_B(\infty) = \sum_{i \leq 3} \gamma_{ij} (z_{ib} c_i^{-m} - 1) = \Delta_B$

(13)

where $E_{coh}(\infty) = N_j z_b E_b$ represents the ideal situation without *CN reduction*. The $z_{ib} = z_i/z_b$ is the normalized *CN* and $E_{ib} = E_i/E_b \cong c_i^{-m}$ is the normalized binding energy per coordinate of a surface atom. For an isolated surface, $\Delta_B < 0$; for an intermixed interface, Δ_B may be positive depending on the strength of interfacial interaction. Therefore, the relative change of $T_C(K_j)$ and activation energy, $E_A(K_j)$ for thermally and mechanically activated process can be expressed as:

$$\frac{\Delta T_C(K_j)}{T_C(\infty)} = \frac{\Delta E_A(K_j)}{E_A(\infty)} = \frac{\Delta E_B(K_j)}{E_B(\infty)} = \Delta_B(K_j)$$
(14)

Interestingly, the critical temperature for sensing operation could be lowered from 970 to 310 K of SrTiO₃ by ball milling to obtain 27 nm-sized powders.⁵⁰ The resistivity of the SrTiO₃ increases when the SrTiO₃ particle size is decreased.⁵¹ Decreasing the particle sizes of ferroelectric BaTiO₃ could lower the T_C to 400 K and the refractive index (dielectric constant), and hence the transmittance of BaTiO₃ infilled SiO₂ photonic crystals, as a consequence.^{52,53} The suppression of the critical temperatures for sensing and phase transition results and the modulation of resistivity and refractive index could be consequences of energy densification and cohesive energy suppression in the surface skin.

2.5.3 Hamiltonian perturbation

The perturbation to the energy density in the relaxed region that contributes to the Hamiltonian upon assembly of the nanosolids is,

$$\begin{aligned}
\Delta_H(K_j) &= \frac{V_{cry}(r, n, N_j)}{V_{cry}(d_0, n, N_j)} - 1 \\
&= \sum_{i \leq 3} \gamma_{ij} \frac{\Delta v(d_i)}{v(d_0)} + \delta_{kj} \\
&= \sum_{i \leq 3} \gamma_{ij} (c_i^{-m} - 1) + \delta_{kj}
\end{aligned}$$

$$\text{where, } \delta_{kj} = \frac{nV(K_j)}{N_j^2 v(d_0)} \quad (15)$$

With the perturbation, the \hat{H}' in eq (3) becomes, $\hat{H}'(\Delta_H) = V_{cry}(r)[1 + \Delta_H(K_j)]$, which dictates the change of not only the E_G width, but also the core-level energy:

$$\frac{\Delta E_G(K_j)}{E_G(\infty)} = \frac{\Delta E_v(K_j)}{E_v(\infty)} = \Delta_H(K_j) \quad (16)$$

where $\Delta E_v(K_j) = E_v(K_j) - E_v(1)$. This relation also applies to other quantities such as the bandwidth and band tails.³³

Most strikingly, without triggering electron-phonon interaction or electron-hole generation, scanning tunneling microscopy/spectroscopy (STM/S) measurement at low temperature revealed that the E_G of Si nanorod varies from 1.1 to 3.5 eV with decreasing the rod diameter from 7.0 to 1.3 nm associated with ~12% Si-Si bond contraction from the bulk value (0.263 nm) to ~0.23 nm. The STS findings concur excitingly with the BOLS premise: CN reduction shortens the remaining bonds of the lower-coordinated atoms spontaneously with an association of E_G expansion.

2.5.4 Electron-phonon coupling

Electron-phonon (e-p) interaction contributes to the processes of photoemission, photoabsorption, photoconduction, and electron polarization that dominates the static dielectric constant. Figure 4 illustrates the effect of e-p coupling and crystal binding on the energy of photoluminescence and adsorbance, E_{PL} and E_{PA} . The energies of the ground state (E_1) and the excited state (E_2) are expressed in parabola forms:³⁴

$$\begin{cases} E_1(q) = Aq^2 \\ E_2(q) = A(q - q_0)^2 + E_G \end{cases} \quad (17)$$

Constant A is the slope of the parabolas. The q is in the dimension of wave-vector. The vertical distance between the two minima is the true E_G that depends uniquely on the crystal potential. The lateral displacement (q_0) originates from the e-p coupling that can be strengthened by lattice contraction. Therefore, the blue shift in the E_{PL} and in the E_{PA} is the joint contribution from crystal binding and e-p coupling.

Figure 4 ([link](#)) Mechanisms for E_{PA} and E_{PL} of a nano-semiconductor, involving crystal binding (E_G) and electron-phonon coupling (W). Insertion illustrates the Stokes shift from E_{PA} to E_{PL} . Electron is excited by absorbing a photon with energy E_G+W from the ground minimum to the excited state and then undergoes a thermalization to the excited minimum, and then transmits to the ground emitting a photon with energy E_G-W .⁵⁴

In the process of carrier formation, or electron polarization,³⁴ an electron is excited by absorbing a photon with E_G+W energy from the ground minimum to the excited state with creation of an electron-hole pair. The excited electron then undergoes a thermalization and moves to the minimum of the excited state, and eventually transmits to the ground and combines with the hole. The carrier recombination is associated with emission of a photon with energy $E_{PL} = E_G - W$. The transition processes (e-h pair production and recombination) follow the rule of momentum and energy conservation though the conservation law may be subject to relaxation for the short ordered nanosolid. Relaxation of the conservation law is responsible for the broad peaks in the PA and PL.

The insertion illustrates the Stokes shift, $2W = 2Aq_0^2$, or the separation from E_{PL} to E_{PA} . The q_0 is inversely proportional to atomic distance d_i , and hence, $W_i = A/(c_i d_i)^2$, in the surface region. Based on this premise, the blue shift of the E_{PL} , the E_{PA} , and the Stokes shift can be correlated to the CN reduction-induced bond contraction:⁵⁴

$$\left. \begin{array}{l} \frac{\Delta E_{PL}(K_j)}{E_{PL}(\infty)} \\ \frac{\Delta E_{PA}(K_j)}{E_{PA}(\infty)} \end{array} \right\} = \frac{\Delta E_G(K_j) \mp \Delta W(K_j)}{E_G(\infty) \mp W(\infty)} \cong \sum_{i \leq 3} \gamma_i [(c_i^{-m} - 1) \mp B(c_i^{-2} - 1)]$$

$$= \Delta_H \mp B \Delta_{e-p}$$

$$\left(B = \frac{A}{E_G(\infty) d^2}; \quad \frac{W(\infty)}{E_G(\infty)} \approx \frac{0.007}{1.12} \approx 0 \right)$$
(18)

Compared with the bulk $E_G(\infty) = 1.12$ eV for silicon, the $W(\infty) \sim 0.007$ eV obtained using tight-binding calculations⁵⁵ is negligible. One can easily calculate the size dependent E_{PL} , E_{PA} , and $E_G = (E_{PL} + E_{PA})/2$ using Eq (18). Fitting the measured data gives the values of m and A for a specific semiconductor.

2.5.5 Mechanical strength

The mechanical yield strength is the strain-induced internal energy deviation that is proportional to energy density or the sum of bond energy per unit volume.¹ Considering the contribution from heating, the strength (stress, flow strength), the Young's modulus, and the compressibility (under compressive stress) or extensibility (under tensile stress) at a given temperature can be expressed by:

$$\begin{aligned}
P_i(z_i, T) &= - \left. \frac{\partial u(r, T)}{\partial V} \right|_{d_i, T} \sim \frac{N_i \eta_i (T_{m,i} - T)}{d_i^\tau} \\
\beta_i(z_i, T) &= - \left. \frac{\partial V}{V \partial P} \right|_T = [Y_i(z_i, T)]^{-1} = \left[-V \left. \frac{\partial u^{2^{-1}}(r, T)}{\partial V^2} \right|_T \right]^{-1} \\
&= \frac{d_i^\tau}{N_i \eta_i (T_{m,i} - T)} = [P_i(z_i, T)]^{-1}
\end{aligned} \tag{19}$$

β is an inverse of dimension of the Young's modulus or the hardness. N_j is the total number of bonds in d^τ volume. If calibrated with the bulk value at T and using the size dependent specific heat, melting point, and lattice parameter, the temperature, bond nature, and size dependent strength and compressibility of a nanosolid will be:

$$\frac{P(K_j, T)}{P(\infty, T)} = \frac{Y(K_j, T)}{Y(\infty, T)} = \frac{\beta(\infty, T)}{\beta(K_j, T)} = \frac{\eta_1(K_j)}{\eta_1(\infty)} \left(\frac{d(\infty)}{d(K_j)} \right)^3 \times \frac{T_m(K_j, m) - T}{T_m(\infty) - T} \tag{20}$$

The bond number density between the circumferential neighbouring atomic layers does not change upon relaxation ($N_i = N_b$). Eq (20) indicates that the mechanical strength is dictated by the value of $T_m(K_j) - T$ and the specific heat per bond. At T far below the T_m , a surface or a nanostructure is harder than the bulk interior. However, the T_m drops with size K_j and therefore, the surface or nanosolid become softer when the $T_m(K_j) - T$ value becomes smaller. This relation has led to quantification of the surface mechanical strength, the breaking limit of a single bond in monatomic chain and the anomalous Hall-Petch relationship in which the mechanical strength decreases with size in a fashion of $D^{-0.5}$ and then deviates at 10 nm from the Hall-Petch relationship.⁴⁹

2.6 Summary

If one could establish the functional dependence of a detectable quantity Q on atomic separation or its derivatives, the size dependence of the quantity Q is then certain. One can hence design a nanomaterial with desired functions based on such prediction. Physical quantities of a solid can be normally categorized as follows:

- (i) Quantities that are directly related to bond length, such as the mean lattice constant, atomic density, and binding energy.
- (ii) Quantities that depend on the cohesive energy per discrete atom, $E_{B,i} = z_i E_i$, such as self-organization growth, thermal stability, Coulomb blockade, critical temperature for liquidation, evaporation and phase transition of a nanosolid and the activation energy for atomic dislocation, diffusion, and bond unfolding.⁵⁶
- (iii) Properties that vary with the binding energy density in the relaxed continuum region such as the Hamiltonian that determines the entire band structure and related properties such as band-gap, core-level energy, photoabsorption and photoemission.
- (iv) Properties that are contributed from the joint effect of the binding energy density and atomic cohesive energy such as mechanical strength, Young's modulus, surface energy, surface stress, extensibility and compressibility of a nanosolid, as well as the magnetic performance of a ferromagnetic nanosolid.

Using the scaling relation and the BOLS correlation, we may derive solutions to predict the size and shape dependence of various properties. Typical samples are given in Table 2 and Figure 5.

Table 2 Summary of functional dependence of various quantities on particle size and derived information. Typical samples of consistency are shown in Figure 5.

Quantity Q	$\Delta Q(K_j)/Q(\infty) = \Delta_q(K_j)$	Refs	Comments
Lattice constant (d)	$\sum_{i \leq 3} \gamma_{ij} (c_i - 1)$	42	Only outermost three atomic layers contribute
Bond energy (E_i) Band gap (E_G) Core-level shift (ΔE_v)	$\sum_{i \leq 3} \gamma_{ij} (c_i^{-m} - 1) = \Delta_H$	29,33	Δ_H - Hamiltonian perturbation
Electron-phonon coupling energy (Stokes shift, W)	$B \sum_{i \leq 3} \gamma_{ij} (c_i^{-2} - 1) = B \Delta_{e-p}$	54	B-constant
Photoemission and photoabsorption energy (E_{PL} , E_{PA})	$\Delta_H \mp B \Delta_{e-p}$	54	$E_G = (E_{PA} + E_{PL})/2$
Critical temperature for phase transition (T_C); activation energy for	$\sum_{i \leq 3} \gamma_{ij} (z_{ib} c_i^{-m} - 1) = \Delta_B$	47,57	Δ_B -Atomic cohesive perturbation

thermally and mechanically activated processes			
Mechanical strength and Yung's modulus of monatomic bond (P, Y)	$\frac{\eta_i d^3 (T_{m,i} - T)}{\eta_b d_i^3 (T_m(\infty) - T)} - 1$	58	η_1 – specific heat per bond T_m – melting point
Inverse Hall-Petch relation; solid-semisolid-liquid transition	$\frac{\eta_1 (K_j) d^3 (T_m(K_j) - T)}{\eta_b d^3 (K_j) (T_m(\infty) - T)} - 1 = \begin{cases} \leq 0, & (\text{semisolid}) \\ -1, & (\text{liquid}) \end{cases}$	49	
Optical phonon frequency (ω)	$\sum_{i \leq 3} \gamma_{ij} (z_{ib} c_i^{-(m/2+1)} - 1)$	59	
Fermi level	$\sum_{i \leq 3} \gamma_{ij} (c_i^{-2\tau/3} - 1)$	60,61	
Dielectric permittivity ($\chi = \epsilon_r - 1$)	$\Delta_d - (\Delta_H - B \Delta_{e-p})$	62	

Figure 5 Comparison of BOLS predictions with measured size dependence of
(a) Lattice contraction of Pr_2O_3 films on Si substrate.⁶³
(b) Atomic cohesive energy of Mo and W.⁶⁴
(c) Mechanical strength (Inverse hall-Petch relationship, IHPR) of TiO_2 ⁶⁵ nanosolids; Straight line is the traditional Hall-Petch relationship (HPR).
(d) T_m suppression of Bi^{66, 67,68,69,70} and CdS,⁷¹ and
(e) T_C suppression of ferromagnetic Fe_3O_4 nanosolids;⁷²
(f) T_C suppression of ferroelectric PbTiO_3 ,⁷³ $\text{SrBi}_2\text{Ta}_2\text{O}_9$,⁷⁴ BaTiO_3 ,⁷⁵ and anti-ferroelectric PbZrO_3 ⁷⁶ nanosolids. High order CN reduction is considered for dipole-dipole interaction.⁵⁷

Figure 6 Comparison of BOLS predations with measured size dependence of
(a) E_G -expansion measured using STS⁷⁷ and optical method, Data -1 ($E_G = E_{PA} - W$),⁷⁸ Data -2 ($E_G = (E_{PL} + E_{PA})/2$)⁷⁹
(b) Core level shift of Au capped with Thiol⁸⁰ and deposited on Octan⁸¹ shows three-dimensional features while core level shift of Au deposited on TiO_2 ⁸² and Pt⁸³ show one-dimensional pattern.

- (c) Raman acoustic frequency shift of $\text{TiO}_2\text{-a}$ and $\text{TiO}_2\text{-b}$ ⁸⁴ $\text{SnO}_2\text{-a}$ ⁸⁵ nanostructures due to interparticle interaction.
- (d) Raman optical frequency shift of CeO_2 ,⁸⁶ $\text{SnO}_2\text{-1}$,⁸⁷ $\text{SnO}_2\text{-2}$,⁸⁵ InP ,⁸⁸ and
- (e) Dielectric suppression of nanosolid silicon with Data 1, 2, and 3,⁸⁹ Data 4 and 5,⁹⁰ and Data-6.⁹¹
- (f) Temperature and size dependence of magnetization.

3 Effect of oxidation

3.1 Bond-band-barrier (BBB) correlation

The BBB correlation mechanism indicates that it is necessary for an atom of oxygen, nitrogen, and carbon to hybridize its *sp* orbitals upon interacting with atoms in solid phase. Because of tetrahedron formation, non-bonding lone pairs, anti-bonding dipoles, and hydrogen-like bonds are produced, which add corresponding features to the DOS of the valence band of the host, as illustrated in Figure 7.⁹² Bond forming alters the sizes and valences of the involved atoms and causes a collective dislocation of these atoms. Alteration of atomic valences roughens the surface, giving rise to corrugations of surface morphology. Charge transportation not only alters the nature of the chemical bond but also produces holes below the E_F and thus creates or enlarges the E_G .⁹³ In reality, the lone-pair-induced metal dipoles often direct into the open end of a surface due to the strong repulsive forces among the lone pairs and among the dipoles as well. This dipole orientation leads to the surface dipole layer with lowered Φ . For a nitride tetrahedron, the single lone pair may direct into the bulk center, which produces an ionic layer at the surface. The ionic surface network deepens the well depth, or increases the Φ , as the host surface atoms donate their electrons to the electron acceptors. For carbide, no lone pair is produced but the weak antibonding feature exists due to the ion-induced polarization. However, hydrogen adsorption neither adds DOS features to the valence band nor expands the E_G as hydrogen adsorption terminates the dangling bond at a surface, which minimizes the midgap impurity DOS of silicon, for instance.³⁴

Figure 7 Oxygen induced *DOS* differences between a compound and the parent metal (upper) or the parent semiconductor (lower). The lone-pair polarized anti-bonding state lowers the Φ and the formation of bonding and anti-bonding generate holes close to E_F of a metal or near the valence band edge of a semiconductor. For carbide, no lone pair features appear but the ion induced antibonding states will remain.

3.2 Experimental evidence

3.2.1 Surface potential barrier and bond geometry

The work function is expressed as: $\Phi = E_0 - E_F(\rho(E)^{2/3})$,⁹⁴ which is the energy separation between the vacuum level, E_0 , and the Fermi energy, E_F . The Φ can be modulated by enlarging the charge density ($\rho(E)$) through lattice contraction or by raising the energy where the DOS is centered via dipole formation.⁶⁰ Dipole formation could lower the Φ of a metal surface by ~ 1.2 eV.¹ The work function varies from site to site with strong localized features. However, if a hydrogen-bond like forms at the surface, the Φ will restore to the original value or even higher because the metal dipoles donate the polarized electrons to the additional electronegative additives to form a ‘+/dipole’ at the surface.¹

Figure 8 shows a typical STM image and the corresponding model for the Cu(001)-(2×1)-O²⁻ phase. The round bright spots of 0.8 ± 0.2 Å in height correspond to the lone pair induced Cu dipoles. In contrast, the protrusion for the clean Cu(110) surface is about 0.15 Å.⁹⁵ Single O-Cu-O strings are formed along the [010] direction associated with every other row missing because of the tetrahedron bond saturation.

Figure 8 STM image [95] and the corresponding models [1] for the surface atomic valencies of Cu(110)-(2×1)-O²⁻. The STM grey-scale is 0.85 Å, much higher than that of metallic Cu on a clean (110) surface (0.15 Å). The single ‘O²⁻ : Cu^{dipole} : O²⁻’ chain zigzagged by the non-bonding lone pairs and composed of the tetrahedron.

Dynamic XRD and very-low-energy electron diffraction (VLEED) optimization have led to quantification of atomic positions that are determined by the bond geometry such as the bond length and bond angles. A simple conversion between atomic position and bond parameters could give the bond geometry for O-Cu examples as shown in Table 3.

Table 3 Geometrical parameters for the Cu₂O tetrahedron deduced from the XRD data of O-Cu(110) phase⁹⁶ and the Cu₃O₂ paired tetrahedra derived from VLEED calculation of O-Cu(001) surface.⁹⁷ Bond contraction with respect to the ideal length of 1.85 Å results from the effect of bond order loss. The “:” represents the lone pair interaction.

Parameters	O-Cu(110)	O-Cu(001)	conclusion
Ionic bond length (Å)	1.675 (Cu ⁺ -O ²⁻)	1.628 (Cu ²⁺ -O ²⁻)	< 1.80
Ionic bond length (Å)	1.675 (Cu ⁺ -O ²⁻)	1.776 (Cu ⁺ -O ²⁻)	< 1.80
Lone pair length (Å)	1.921 (Cu ^p :O ²⁻)	1.926 (Cu ^p :O ²⁻)	~ 1.92

Ionic bond angle (°)	102.5	102.0	< 104.5
Lone pair angle (°)	140.3	139.4	~ 140.0

3.2.2 Valence density of states

Oxygen derived DOS features can be detected using scanning tunneling spectroscopy (STS) and ultra-violet photoelectron spectroscopy (UPS). The STS spectra in Figure 9 for an O-Cu(110) surface⁹⁵ revealed the lone pair and dipole features. Spectrum A was taken from the clean Cu(110) surface while B and C were taken from, respectively, the site above the bright spot (dipole) and the site between two bright spots along a ‘O²⁻ : Cu^{dipole} : O²⁻’ chain at the Cu(110)-(2×1)-O²⁻ surface. On the clean surface, empty DOS of 0.8 ~ 1.8 eV above E_F are resolved and no extra DOS structures are found below E_F. The STS spectra recorded from the Cu(110)-(2×1)-O²⁻ islands reveal that the original empty-DOS above E_F are partially occupied by electrons upon chemisorption, which result in a slight shift of the empty DOS to higher energy. Additional DOS features are generated around -2.1 eV below the E_F. The sharp features around -1.4 eV have been detected with angular-resolved photoelectron spectroscopy (ARPES)⁹⁸ and with the de-excitation spectroscopy of metastable atoms.⁹⁹ The DOS for Cu - 3d electrons are between -2 and -5 eV,¹⁰⁰ and the O-Cu bonding derivatives are around the 2p-level of oxygen, -5.6 ~ -7.8 eV below E_F.¹⁰¹ The DOS features for Cu-3d and O-Cu bonding are outside the energy range of the STS (E_F ± 2.5 eV). The band-gap-expansion mechanism implies that it is possible to discover or invent new sources for light emission with a desired wavelength by controlling the extent of catalytic reaction. Intense blue-light emission from [b(Zr_xTi_{1-x})O₃] ceramics sample under Ar⁺ ultraviolet (UV) irradiation could be direct evidence for this mechanism.¹⁰²

It has been found that the crystal-geometry and the surface-morphology may vary from surface to surface and from material to material, the oxygen-derived DOS features are substantially the same in nature, as summarized in Table 4. The O-derived DOS features include oxygen-metal bonding (- 5 ~ -8 eV), nonbond lone-pair of oxygen (- 1 ~ -2 eV), holes of metal ions (~ E_F) and antibonding metal-dipole states (> E_F).

Figure 9 (a) STS profiles of a Cu(110) surface [95] with and without chemisorbed oxygen. Spectra in panel (a) were obtained (A) at a metallic region, (B) on top of, and, (C) between protrusions of the ‘O²⁻ : Cu^{dipole} : O²⁻’ chain [92] on the Cu(110)-(2×1)-O²⁻ surface. (b) Oxygen derived DOS features (shaded areas) in the valence band of O-Pd(110) [103] and O-Cu(110) [104] surfaces. Although the microscopy and crystallography of these two systems are quite different the PES

features are substantially the same. Slight difference in the feature positions results from the difference in electronegativity. Features around $-1 \sim -2$ eV and $-5 \sim -8$ eV correspond to the nonbonding lone pairs and the O sp-hybrid bond states, respectively.

Table 4 Oxygen-derived DOS features adding to the valence band of metals (unit in eV). Holes are produced below E_F . All the data were probed with angular-resolved photoelectron spectroscopy unless otherwise indicated.

Oxide surfaces	Methods	Anti-bond dipole	Lone pair	O-M bond
		$> E_F$	$< E_F$	$< E_F$
O-Cu(001) ^{105,106}			-1.5 ± 0.5	-6.5 ± 1.5
	VLEED ¹	1.2	-2.1	
O-Cu(110) ^{98, 104,107,108}		~ 2.0	-1.5 ± 0.5	-6.5 ± 1.5
	STS ⁹⁵	1.3 ± 0.5	-2.1 ± 0.5	
O-Cu(poly) ¹⁰⁰			-1.5	-6.5 ± 1.5
O-Cu/Ag(110) ¹⁰⁹			-1.5	-3.0; -6.0
O-Rh(001) ¹¹⁰	DFT	1.0	-3.1	-5.8
O-Pd(110) ¹¹¹			-2.0 ± 0.5	-4.5 ± 1.5
O-Gd(0001) ¹¹²			-3.0	-6.0
O-Ru(0001) ¹¹³			-1.0 ± 1.0	-5.5 ± 1.5
O-Ru(0001) ¹¹⁴			-0.8	-4.4
O-Ru(0001) ¹¹⁵	Ab initio	1.5	-4	-5.5, -7.8
O-Ru(0001) ¹¹⁶		1.7	-3.0	-5.8
O-Ru(10 $\bar{1}$ 0) ¹¹⁷	DFT	2.5	-2 \sim -3.0	-5.0
O-Co(Poly) ¹¹⁸			-2.0	-5.0
O-diamond (001) ¹¹⁹			-3.0	
(O, S)-Cu(001) ¹²⁰			-1.3	-6.0
(N, O, S)-Ag(111) ¹²¹			-3.4	-8.0

3.2.3 Lone pair interaction

A direct determination of the lone pair interaction is to measure the frequency of vibration in metal oxide surfaces using Raman and high resolution electron energy loss spectroscopy (EELS)^{122,123,124} in the frequency range below 1000 cm^{-1} or the shift energy of ~ 50 meV. Typical Raman spectra in Figure 10 show the lone pair vibration features in Al_2O_3 and TiO_2 powders.¹²⁵ The energy of the stretching vibration of O-M in EELS around 50 meV coincides with the energy of hydrogen bond detected using infrared and Raman spectroscopy from H_2O , protein, and DNA.¹²⁶ The energy for an

ionic bond is normally around 3.0 eV and the energy for a Van der Waals bond is about 0.1 eV. The ~0.05 eV vibration energies correspond to the weak non-bonding interaction between the host dipole and the oxygen adsorbate.

Figure 10 Low-frequency Raman shifts indicate that weak bond interaction exists in Ti and Al oxides, which correspond to the non-bonding electron lone pairs generated during the *sp*-orbital hybridization of oxygen.

A nuclear inelastic scattering of synchrotron radiation measurement¹²⁷ revealed that additional vibrational DOS present at energies around 18 meV and 40-50 meV of oxide-capped nanocrystalline α -Fe (6 – 13 nm sizes) to the modes of the coarse-grained α -Fe. The 50 meV DOS corresponds apparently to the lone pair states while the 18 meV modes could be attributed to intercluster interaction that should increase with inverse of particle size (Figure 6c).

3.2.4 Bond forming kinetics

The spectral signatures of LEED, STM, PES/STS, TDS and EELS can be correlated to the chemical bond, surface morphology, and valence DOS and the bond strength, which enables the kinetics of oxide tetrahedron formation to be readily understood. It has been found general that an oxide tetrahedron forms in four discrete stages: (i) O^{1-} dominates initially at very low oxygen dosage; (ii) O^{2-} -hybridization begins with lone pair and dipole formation upon second bond formation; (iii) interaction develops between lone pairs and dipoles, and finally, (iv) H-bond like forms at higher dosages. These processes give rise to the corresponding DOS features in the valence band and modify the surface morphology and crystallography, accordingly. Therefore, the events of *sp*-hybrid bonding, non-bonding lone pair, anti-bonding dipole and the H-like bonding are essential in the electronic process of oxidation, which should determine the performance of an oxide.

3.3 Summary

It is essential that an oxygen atom hybridizes its *sp* orbitals upon reacting with atoms in solid phase. In the process of oxidation, electronic holes, non-bonding lone pairs, anti-bonding dipoles and hydrogen-like bonds are involved, which add corresponding density-of-states features to the valence band of the host. Formation of the basic oxide tetrahedron, and consequently, the four discrete stages of bond forming kinetics and the oxygen-derived DOS features, are intrinsically common for all the analyzed systems though the patterns of observations may vary from situation to situation. What differs one oxide surface from another in observations are: (i) the site selectivity of the oxygen

adsorbate, (ii) the order of the ionic bond formation and, (iii) the orientation of the tetrahedron at the host surfaces. The valencies of oxygen, the scale and geometrical orientation of the host lattice and the electronegativity of the host elements determine these specific differences extrinsically.

Knowing the bonding events and their consequences would help us to scientifically design and synthesis of oxide nanostructures with desired functions. Predictions of the functions and potential applications of the bonding events at a surface with chemisorbed oxygen are summarized in Table 5. Oxidation modifies directly the occupied valence DOS by charge transportation or polarization, in particular the band gap and work function. The involvement of the often-overlooked events of lone pair and dipoles may play significant roles in many aspects of the performance of an oxide. The bond contraction is not limited to an oxide surface but it happens at any site, where the atomic *CN* reduces.

Table 5 Summary of special bonding events and potential applications of oxide nanomaterials.

Events	Functions	Potential Applications
Anti-bonding (dipole) $> E_F$	Work function-reduction ($\Delta\phi$)	Cold-cathode Field emission
Holes $< E_F$	Band-gap expansion	PL blue-shift UV detection
Nonbonding (Lone pair) $< E_F$	Polarization of metal electrons	High elasticity Raman and Far-IR low frequency activity
H- or CH- like bond	$\Delta\phi$ - Recovery	Bond network stabilization
Bond Order loss	BOLS correlation charge, mass and energy densification Cohesive energy Hamiltonian	Origin for the tunability of nano-solids

4 Conclusion

The impact of the often-overlooked event of atomic CN reduction is indeed tremendous, which unifies the performance of a surface, a nanosolid and a solid in amorphous state consistently in terms of bond relaxation and its consequences on bond energy. The unusual behavior of a surface and a nanosolid has been consistently understood and systematically formulated as functions of atomic CN reduction and its derivatives on the atomic trapping potential, crystal binding intensity, and electron-phonon coupling. The properties include the lattice contraction (nanosolid densification and surface relaxation), mechanical strength (resistance to both elastic and plastic deformation), thermal stability (phase transition, liquid-solid transition, and evaporation), and lattice vibration (acoustic and optical phonons). They also cover photon emission and absorption (blue shift), electronic structures (core level disposition and work function modulation), magnetic modulation, dielectric suppression, and activation energies for atomic dislocation, diffusion, and chemical reaction. Structural miniaturization has formed indeed a new freedom that allows us to tune the physical properties that are initially non-variable for the bulk chunks by simply changing the shape and size to make use of the effect of atomic CN reduction.

The effect of size reduction and the effect of oxidation enhance each other in many aspects such as the charge localization, band gap expansion, and work function modulation. For instances, the enhancement of energy density enlarges the band gap intrinsically while charge transport from metal to oxygen enlarges the E_G extrinsically by electron-hole production; both charge polarization in the process of reaction and densification in the process of size reduction lower the work function.

It is the practitioner's view that we are actually making use of the effect of bond order loss in size reduction and the effect of bond nature alteration in oxidation in dealing with oxide nanomaterials. Grasping with the factors controlling the process of bond making, breaking and relaxing would be more interesting and rewarding.

Fig.1

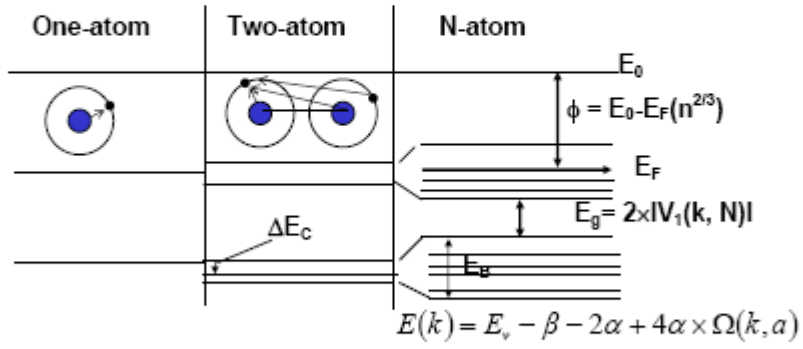
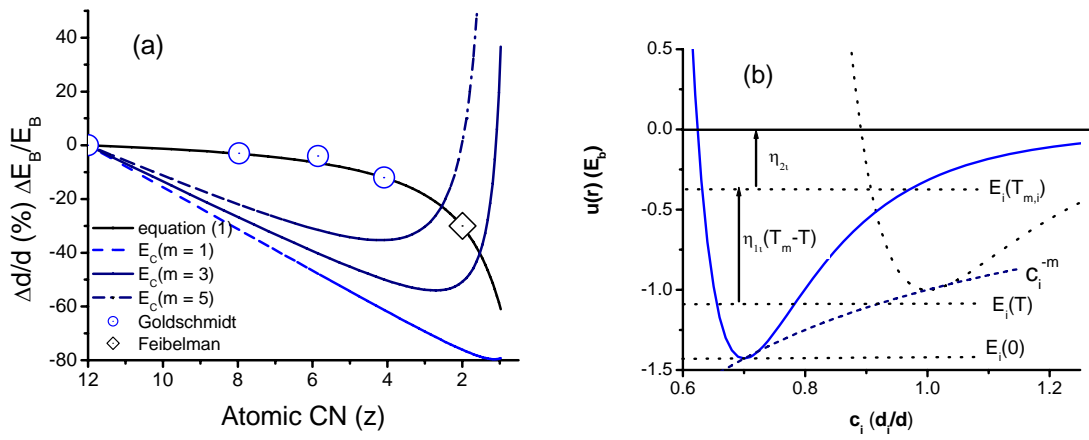
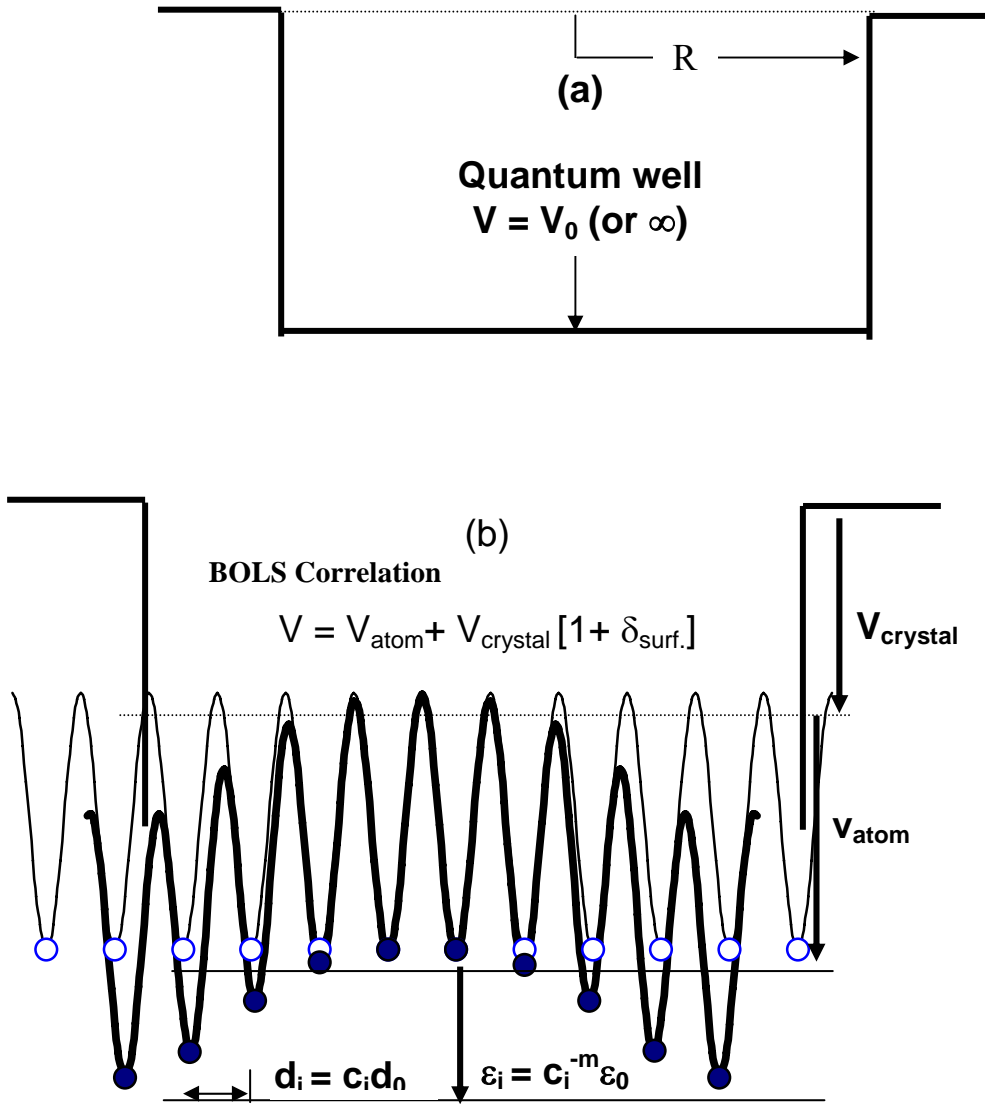


Fig-01



Fg-02



Fg-03

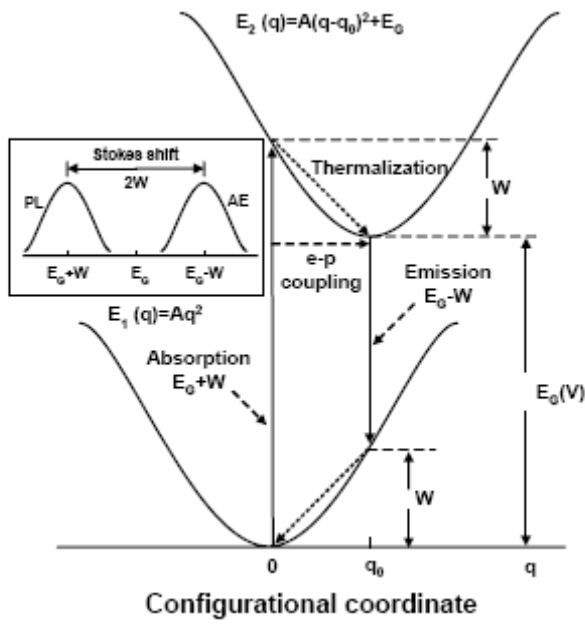
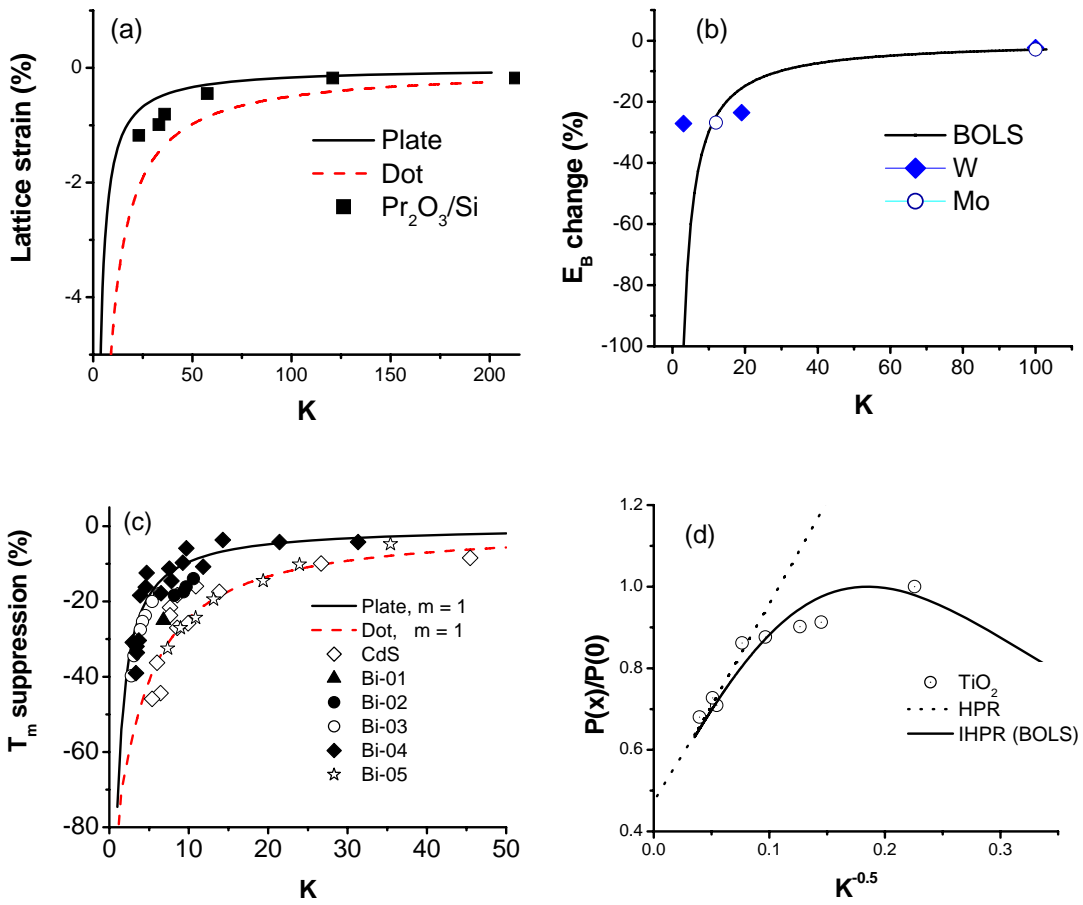


Fig-04



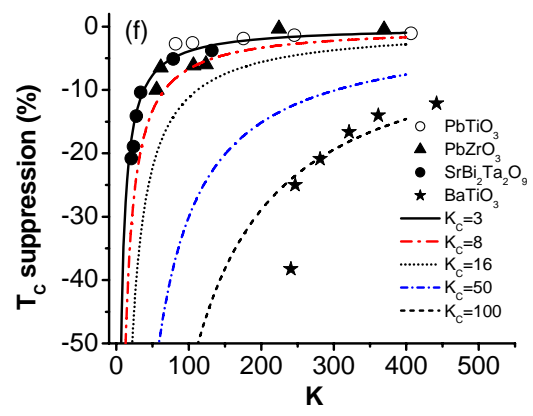
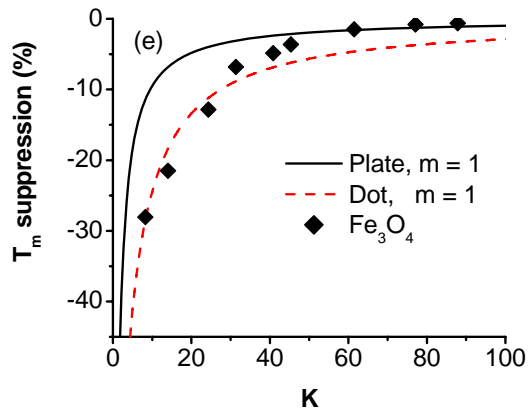
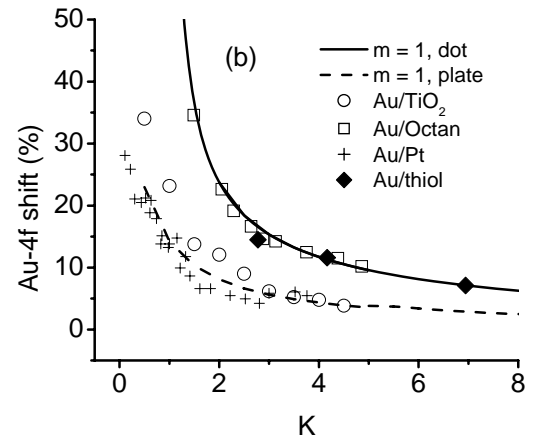
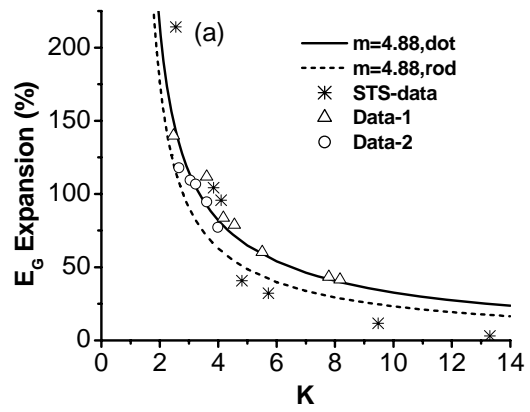


Fig-05



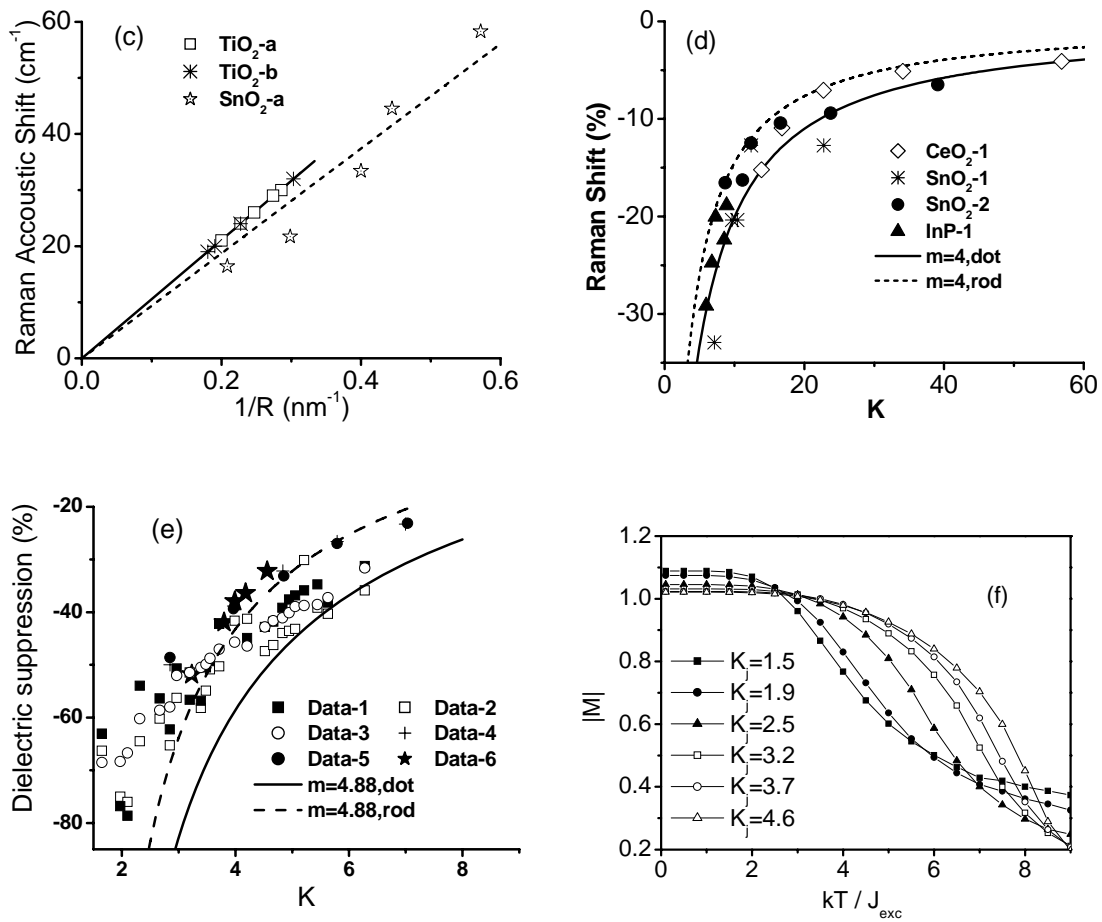


Fig-06

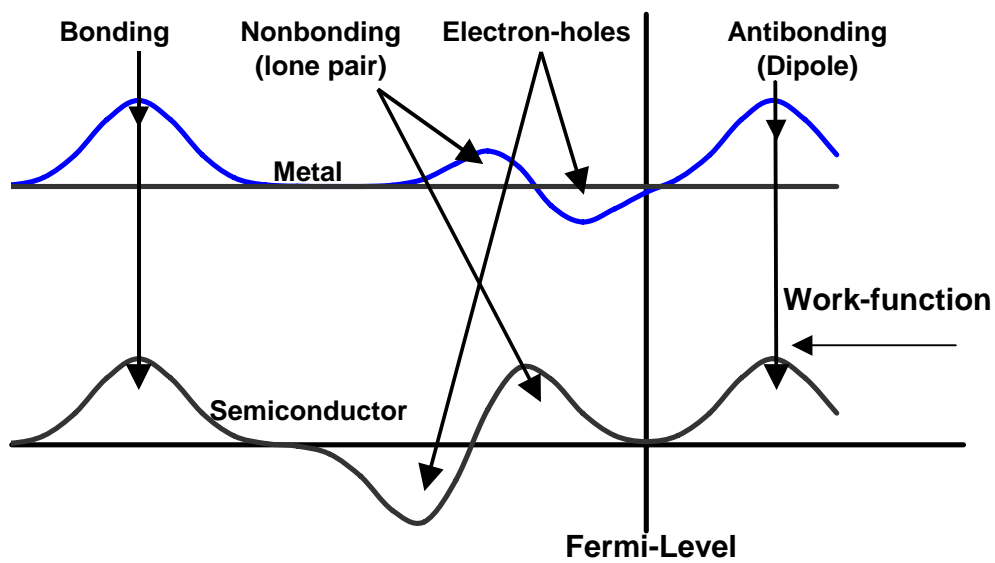


Fig-07

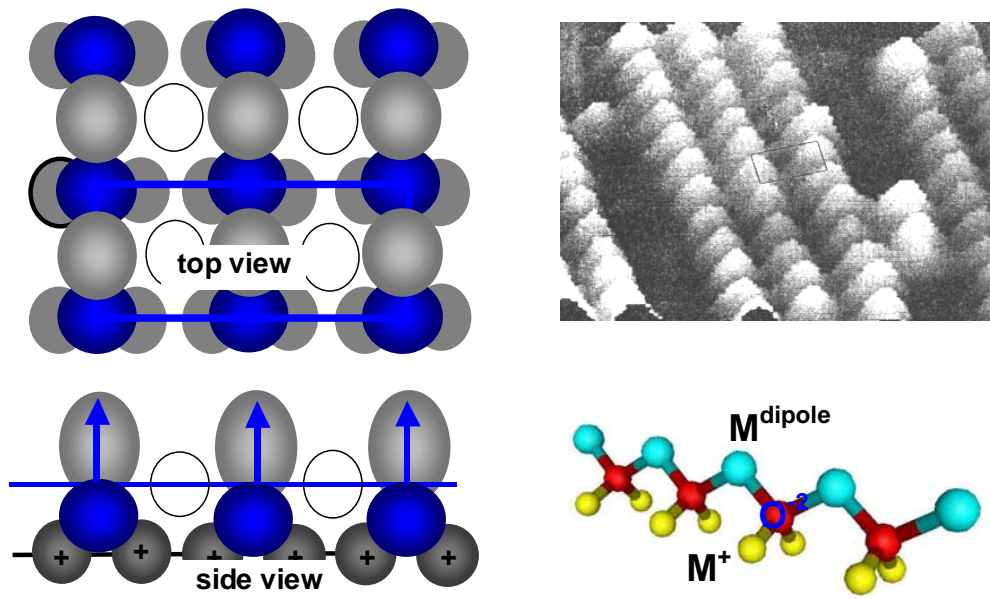


Fig-08

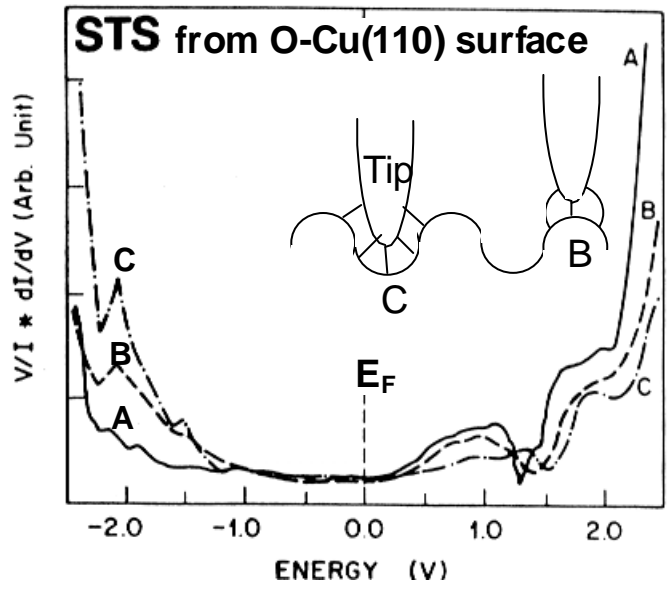
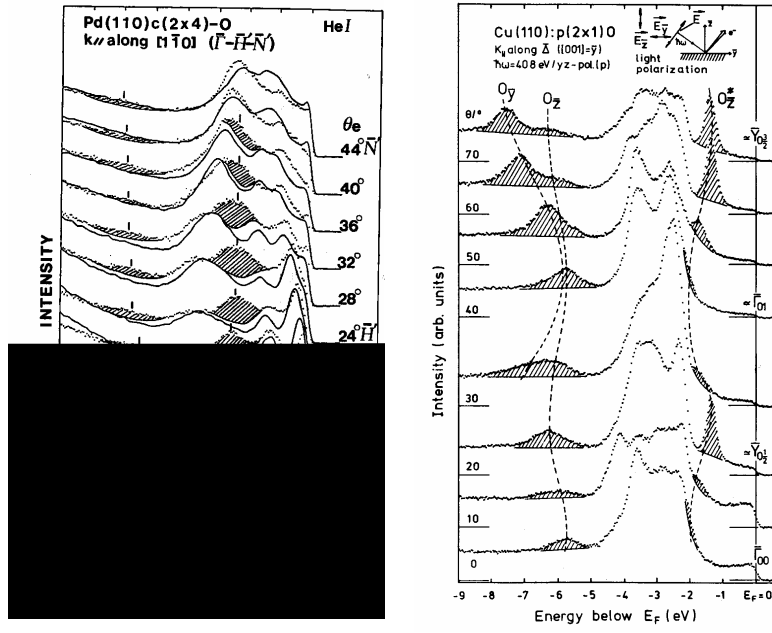


Fig-09

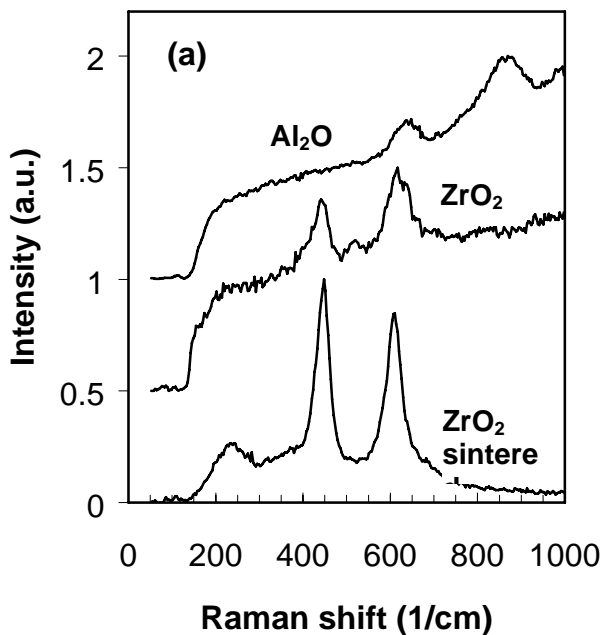
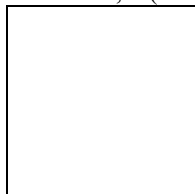


Fig.10

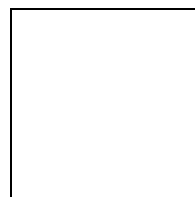
References

- [1] Sun CQ, Oxidation electronics, bond-band-barrier correlation and its applications, *Prog Mater Sci* 48, 521-685 (2003).
- [2] Wintterlin J, Behm RJ, In the Scanning Tunnelling Microscopy I Chapter 4, eds Günthert HJ and Wiesendanger R, Springer-Verlag, Berlin (1992).
- [3] Fernandez-Garcia M, Martinez-Arias A, Hanson JC, Rodriguez JA, Nanostructured oxides in chemistry, Characterization and properties, *CHEM REV* 104 (9) 4063-4104 (2004).
- [4] Qin GG, Song HZ, Zhang BR, Lin J, Duan JQ, and Yao GQ, Experimental evidence for luminescence from silicon oxide layers in oxidized porous silicon *Phys Rev B* 54, 2548-2555 (1996).
- [5] Koch F, Petrova-Koch V, Muschik T, Nikolov A and Gavrilenko V, in *Micrystalline Semiconductors, Materials Science and Devices*, Materials research Society, Pittsburgh, PA, 283, 197 (1993).
- [6] Wang X, Qu L, Zhang J, Peng X, and Xiao M, Surface-Related Emission in Highly Luminescent CdSe Quantum Dots, *Nanolett* 3, 1103-1106 (2003).
- [7] Prokes SM, Surface and optical properties of porous silicon *J Mater Res* 11, 305-319 (1996).
- [8] Iwayama TS, Hole DE, and Boyd IW, Mechanism of photoluminescence of Si nanocrystals in SiO₂ fabricated by ion implantation, the role of interactions of nanocrystals and oxygen, *J Phys Condens Matter* 11, 6595-6604 (1999).
- [9] Trwoga PF, Kenyon AJ, and Pitt CW, Modeling the contribution of quantum confinement to luminescence from silicon nanoclusters, *J Appl Phys* 83, 3789-94 (1998).
- [10] Efros AL and Efros AL, Interband absorption of light in a semiconductor sphere, *Sov Phys Semicond* 16, 772-5 (1982).
- [11] Brus JE, On the development of bulk optical properties in small semiconductor crystallites, *J Lumin* 31, 381-4 (1984).
- [12] Kayanuma Y, Quantum-size effects of interacting electrons and holes in semiconductor microcrystals with spherical shape, *Phys Rev B* 38, 9797-9805 (1988).
- [13] Ekimov AI and Onushchenko AA, Quantum size effect in the optical spectra of semiconductor microcrystals, *Sov Phys Semicond* 16, 775-778 (1982).

-
- [14] Glinka YD, Lin SH, Hwang LP, Chen YT, Tolk NH, Size effect in self-trapped exciton photoluminescence from SiO₂-based nanoscale materials *Phys Rev B* 64, 085421 (2001).
- [15] Lindemann FA, *Z Phys* 11, 609 (1910).
- [16] Born M, *J Chem Phys* 7, 591 (1939).
- [17] Buffat P and Borel JP, Size effect on the melting temperature of gold particles, *Phys Rev A* 13, 2287-98 (1976).
- [18] Pawlow P, *Z Phys Chem Munich* 65, 1 (1909).



- [19] Vekhter B and Berry RS, Phase coexistence in clusters, an "experimental" isobar and an elementary model, *J Chem Phys* 106, 6456-9 (1997).
- [20] Reiss H, Mirabel P, and Whetten RL, Capillarity theory for the "coexistence" of liquid and solid clusters, *J Phys Chem* 92, 7241-6 (1988).
- [21] Sakai H, Surface-induced melting of small particles, *Surf Sci* 351, 285-91 (1996).
- [22] Ubbelohde AR, *The molten State of Materials* Wiley, New York, 1978.
- [23] Vanfleet RR and Mochel JM, Thermodynamics of melting and freezing in small particles, *Surf Sci* 341, 40-50 (1995).
- [24] Nanda KK, Sahu SN, and Behera SN, Liquid-drop model for the size-dependent melting of low-dimensional systems, *Phys Rev A* 66, 013208 (2002).
- [25] Jiang Q, Liang LH, and Li JC, Thermodynamic superheating and relevant interface stability of low-dimensional metallic crystals, *J Phys Condens Matt* 13, 565-71 (2001).
- [26] Jiang Q, Liang LH, and Zhao M, Modelling of the melting temperature of nano-ice in MCM-41 pores, *J Phys Condens Matt* 13, L397-401 (2001).
- [27] Jiang Q, Zhang Z, and Li JC, Superheating of nanocrystals embedded in matrix, *Chem Phys Lett* 322, 549-552 (2000).
- [28] Vallee R, Wautelet M, Dauchot JP, and Hecq M, Size and segregation effects on the phase diagrams of nanoparticles of binary systems *Nanotechnology* 12, 68-74 (2001).
- [29] Sun CQ, Surface and nanosolid core-level shift: impact of atomic coordination number imperfection, *PHYS REV B* 69, 045105 (2004).
- [30] Sun CQ, Gong HQ, Hing P, Behind the quantum confinement and surface passivation of nanoclusters, *SURF REV LETT* 6, L171-176 (1999).
- [31] Rao CNR, Kulkarni GU, Thomas PJ, Edwards PP, Size-dependent chemistry, Properties of nanocrystals, *Chem Euro J* 8, 28-35 (2002).



- [32] Aiyer HN, Vijayakrishnan V, Subbanna GN, Rao CNR, Investigations of Pd clusters by the combined use of HREM, STM, high-energy spectroscopies and tunneling conductance measurements, *Surf Sci* 313, 392-398 (1994).
- [33] Sun CQ, Chen TP, Tay BK, Li S, Huang H, Zhang YB, Pan LK, Lau SP and Sun XW, An extended 'quantum confinement' theory, surface-coordination imperfection modifies the entire band structure of a nanosolid, *J PHYS D* 34, 3470-3479 (2001).
- [34] Street RA, *Hydrogenated amorphous silicon* Cambridge University Press, Cambridge, 1991.
- [35] Zhong WH, Sun CQ, Li S, Bai HL, Jiang EY, Impact of bond order loss on surface and nanosolid magnetism, *ACTA MATERIALIA*, IN PRESS.
- [36] Goldschmidt VM, *Ber Deut Chem Ges* 1927, 60, 1270.
- [37] Pauling L, Atomic radii and interatomic distances in metals, *J Am Chem Soc* 69, 542-553 (1947).
- [38] Sinnott MJ, *The solid state for engineers*, Wiley and Sons, New York, 1963.
- [39] Shpyrko OG, Grigoriev AY, Steimer C, Pershan PS, Lin B, Meron M, Graber T, Gerbhardt J, Ocko B, Deutsch M, *Phys Rev B* 70, 224206 (2004)

⁴⁰ Mahnke H.-E., Haas H., Holub-Krappe E., Koteski V., Novakovic N., Fochuk P. and Panchuk O, Lattice distortion around impurity atoms as dopants in CdTe, *Thin Solid Films* 480-481, (2005) 279-282.

-
- [41] Feibelman PJ, Relaxation of hcp(0001) surfaces, A chemical view, *Phys Rev B* 53, 13740-13746 (1996).
- [42] Sun CQ, Tay BK, Zeng XT, Li S, Chen TP, Zhou J, Bai HL, Jiang EY, Bond-order-length-strength (BOLS) correlation mechanism for the shape and size dependency of a nanosolid *J PHYS CONDENS MATT* 2002, 14, [7781-95](#).
- [43] Sun CQ, Bai HL, Tay BK, Li S, Jiang EY, Dimension, strength, and chemical and thermal stability of a single C-C bond in carbon nanotubes, *J Phys Chem B* 107, 7544-7546 (2003).
- [44] Chen TP, Liu Y, Sun CQ, et al, Core-level shift of Si nanocrystals embedded in SiO₂ matrix, *J PHYS CHEM B* 108, 16609-16611 (2004).
- [45] Sun CQ, Li CM, Bai HL, Jiang EY, Bond nature evolution in atomic clusters, *J PHYS CHEM B IN PRESS*
- [46] Bahn SR and Jacobsen KW, Chain Formation of Metal Atoms, *Phys Rev Lett* 87, 266101 (2001).
- [47] Sun CQ, Wang Y, Tay BK, Li S, Huang H, Zhang YB, Correlation between the melting point of a nanosolid and the cohesive energy of a surface atom, *J Phys Chem B* 106, 10701-10705 (2002).
- [48] Kocks UF, Argon AS, and Ashby AS, *Prog Mater Sci* 19, 1 (1975).
- [49] Sun CQ, Li S, Li CM, Impact of bond-order loss on surface and nanosolid mechanics, *J Phys Chem B* 109, 415-23 (2005).
- [50] Hu Y, Tan OK, Cao W, Zhu W, Fabrication and characterization of nano-sized SrTiO₃-based oxygen sensor for near-room temperature operation, *IEEE Sensors J* 2004, in press
- [51] Hu Y, Tan OK, Pan JS, Yao X, A new form of nano-sized SrTiO₃ material for near human body temperature oxygen sensing applications, *J Phys Chem B* 108, 11214-11218 (2004).
- [52] Zhou J, Sun CQ, Pita K, Lam YL, Zhou Y, Ng SL, Kam CH, Li LT, Gui ZL, Thermally tuning of the photonic band-gap of SiO₂ colloid-crystal infilled with ferroelectric BaTiO₃, *Appl Phys Lett* 78, 661-663 (2001).
- [53] Li B, Zhou J, Hao LF, Hu W, Zong RL, Cai MM, Fu M, Gui ZL, Li LT, Li Q, Photonic band gap in (Pb,La)(Zr,Ti)O₃ inverse opals, *Appl Phys Lett* 82, 3617-3619 (2003).
- [54] Pan LK, Sun CQ, Coordination imperfection enhanced electron-phonon interaction in nanosolid silicon, *J APPL PHYS* 95, 3819-3821 (2004).
- [55] Sanders GD, and Chang YC, Theory of optical properties of quantum wires in porous silicon, *Phys Rev B* 45, 9202-9213 (1992).
- [56] Tománek D, Mukherjee S, and Bennemann KH, Simple theory for the electronic and atomic structure of small clusters, *Phys Rev B* 28, 665-73 (1983).
- [57] Sun CQ, Zhong WH, Li S, Tay BK, Bai HL, Jiang EY, Coordination imperfection suppressed phase stability of ferromagnetic, ferroelectric, and superconductive nanosolids, *J PHYS CHEM B* 108(3), [1080-1084](#) (2004).
- [58] Sun CQ, Li C, and Li S, Breaking limit of atomic distance in an impurity-free monatomic chain, *PHYS REV B* 69, 245402 (2004).
- [59] Sun CQ, Pan LK, Li CM, Elucidating Si-Si dimer vibration from the size-dependent Raman shift of nanosolid Si, *J PHYS CHEM B* [108\(11\), L3404-3406](#) (2004).
- [60] Zheng WT, Sun CQ, Tay BK, Modulating the work function of carbon by O and N addition and nanotip formation, *SOLID STATE COMMUN* 128, [381-384](#) (2003).
- [61] Poa CHP, Smith RC, Silva SRP, Sun CQ, Influence of mechanical stress on electron field emission of multi-walled carbon nanotube-polymer composites, *J VAC SCITECHNOL B* 23, 698-701 (2005).
- [62] Pan LK, Sun CQ, Dielectric suppression of nanosolid Si, *NANOTECHNOLOGY* [15, 1802-1806](#) (2004).
- [63] Liu JP, Zaumseil P, Bugiel E, and Osten HJ, Epitaxial growth of Pr₂O₃ on Si(111) and the observation of a hexagonal to cubic phase transition during postgrowth N₂ annealing, *Appl Phys Lett* 79, 671- 673 (2001).
- [64] Kim HK, Huh SH, Park JW, Jeong JW, Lee GH, The cluster size dependence of thermal stabilities of both molybdenum and tungsten nanoclusters, *Chem Phys Lett* 354, 165-72 (2002).
- [65] Höfler H J, and Averbach RS, *Scripta Metall Mater* 24, 2401 (1990).
- [66] Peppiat SJ, *Proc R Soc London Ser A* 345, 401 (1975).
- [67] Itoigawa H, Kamiyama T, and Nakamura Y, Bi precipitates in Na₂O–B₂O₃ glasses, *J Non-Cryst Solids* 210, 95-100 (1997).
- [68] Kellermann G and Craievich AF, Structure and melting of Bi nanocrystals embedded in a B₂O₃-Na₂O glass, *Phys Rev B* 65, 134204 (2002).
- [69] Allen GL, Gile WW, Jesser WA, Melting temperature of microcrystals embedded in a matrix *Acta Metall* 28, 1695-1701 (1980).
- [70] Skripov VP, P KoverdaV, and Skokov VN, Size effect on melting of small particles *Phys Status Solidi A* 66, 109-118 (1981).
- [71] Goldstein N, Echer CM, Alivistos AP, Melting in semiconductor nanocrystals, *Science* 256, 1425-1427 (1992).

-
- [72] Sadeh B, Doi M, Shimizu T, and Matsui MJ, Dependence of the Curie temperature on the diameter of Fe₃O₄ ultra-fine particles, *J Magn Soc Jpn* 24, 511-514 (2000).
- [73] Zhong WL, Jiang B, Zhang PL, Ma JM, Cheng HM, Yang ZH, and Li LX, Phase transition in PbTiO₃ ultrafine particles of different sizes, *J Phys Condens Matt* 5, 2619-2624 (1993).
- [74] Yu T, Shen ZX, Toh WS, Xue JM, and Wang JJ, Size effect on the ferroelectric phase transition in SrBi₂Ta₂O₉ nanoparticles, *J Appl Phys* 94, 618-620 (2003).
- [75] Uchina K, Sadanaga Y, Hirose T, *J Am Ceram Soc* 72, 1555 (1999).
- [76] Chattopadhyay S, Ayyub P, Palkar VR, Gurjar AV, Wankar RM, Multani, M Finite-size effects in antiferroelectric PbZrO₃ nanoparticles *J Phys Condens Matt* 9, 8135-8145 (1997).
- [77] Ma DDD, Lee CS, Au FCK, Tong SY, and Lee ST, Small-diameter silicon nanowire surfaces, *Science* 299, 1874-1877 (2003).
- [78] Campbell IH, and Fauchet PM, Effects of microcrystal size and shape on the phonon Raman spectra of crystalline semiconductors, *Solid State Commun* 58, 739-41 (1986).
- [79] Pan LK, Sun CQ, Tay BK, Chen TP, and Li S, Photoluminescence of Si nanosolids near the lower end of the size limit *J Phys Chem B* 106, 11725-11727 (2002).
- [80] Zhang P and Sham TK, X-Ray Studies of the Structure and Electronic Behavior of Alkanethiolate-Capped Gold Nanoparticles, The Interplay of Size and Surface Effects, *Phys Rev Lett* 90, 245502 (2003).
- [81] Ohgi T and Fujita D, Consistent size dependency of core-level binding energy shifts and single-electron tunneling effects in supported gold nanoclusters *Phys Rev B* 66, 115410 (2002).
-
- [82] Howard A, Clark DNS, Mitchell CEJ, Egdell RG, and Dhanak VR, Initial and final state effects in photoemission from Au nanoclusters on TiO₂(110), *Surf Sci* 518, 210-224 (2002).
- [83] Salmon M, Ferrer S, Jazzar M and Somojai GA, Core- and valence-band energy-level shifts in small two-dimensional islands of gold deposited on Pt(100): The effect of step-edge, surface, and bulk atoms, *Phys Rev B* 28, 1158-60 (1983).
- [84] Gotić M, Ivanda M, Sekulić A, Musić S, Popović S, Turković A, Furić K, *Mater Lett* 28 225 (1996).
- [85] Dieguez A, Romano-Rodríguez A, Vila A, and Morante JR, The complete Raman spectrum of nanometric SnO₂ particles, *J Appl Phys* 90, 1550-1557 (2001).
- [86] Spanier JE, Robinson RD, Zhang F, Chan SW, and Herman IP, Size-dependent properties of CeO₂ nanoparticles as studied by Raman scattering, *Phys Rev B* 64, 245407 (2001).
- [87] Shek CH, Lin GM and Lai JKL, Effect of oxygen deficiency on the Raman spectra and hyperfine interactions of nanometer SnO₂ Nanosructured *Mater* 1999, 11, 831–835 (1999).
- [88] Seong MJ, Micic OI, Nozik AJ, Mascarenhas A, and Cheong HM, Size-dependent Raman study of InP quantum dots, *Appl Phys Lett* 82, 185-187 (2003).
- [89] Lannoo M, Delerue C, and Allan G, Screening in Semiconductor Nanocrystallites and Its Consequences for Porous Silicon, *Phys Rev Lett* 74, 3415-8 (1995).
- [90] Wang LW and Zunger A, Dielectric Constants of Silicon Quantum Dots *Phys Rev Lett* 73, 1039-1042 (1994).
- [91] Pan LK, Huang HT, Sun CQ, Dielectric transition and relaxation of nanosolid silicon, *J Appl Phys* 94, 2695-700 (2003).
- [92] Sun CQ and Li S, Oxygen derived DOS features in the valence band of metals. *Surf Rev Lett* 7, L213-217 (2000).
- [93] Sun CQ, A model of bonding and band-forming for oxides and nitrides, *Appl Phys Lett* 72, 1706-1708 (1998).
- [94] Wales DJ, Structure, dynamics, and thermodynamics of clusters, tales from topographic potential surfaces, *Science* 271, 925-9 (1996).
- [95] Chua FM, Kuk Y and Silverman PJ, Oxygen chemisorption on Cu(110): an atomic view by scanning tunneling microscopy, *Phys Rev Lett* 63, 386-389 (1989).
- [96] Feidenhans'l R, Grey F, Johnson R.L, Mochrie S.G.J, Bohr J and Nielsen M, Oxygen chemisorption on Cu(110): A structural determination by x-ray diffraction, *Phys Rev B* 41, 5420-5423 (1990).
- [97] Sun CQ and Bai CL, A model of bonding between oxygen and metal surfaces, *J Phys Chem Solids* 58, 903-912 (1997).
- [98] Jacob W, Dose V and Goldmann A, Atomic adsorption of oxygen on Cu(111) and Cu(110), *Appl Phys A* 41, 145-150 (1986).

-
- [99] Sesselmann W, Conrad H, Ertl G, Küppers J, Woratschek B, Haberland H, Probing the local density of states of metal surfaces by de-excitation of metastable noble-gas atoms, *Phys Rev Lett* 50, 446-450 (1983).
- [100] Belash VP, Klimova IN, Kormilets VI, Trubjtsjn VY and Finkelstein LD, Transformation of the electronic structure of Cu into Cu₂O in the adsorption of oxygen, *Surf Rev Lett* 6, 383-388 (1999).
- [101] Courths R, Cord B, Wern H, Saalfeld H, Hüfner S, Dispersion of the oxygen-induced bands on Cu(110)-an angle-resolved UPS study of the system p(2 × 1)O/Cu(110), *Solid State Commun* 63, 619-623 (1987).
- [102] Jin D., Hing P. and Sun C. Q., *J. Phys. D: Appl. Phys.* 33, 744-752 (2000). ‘Growth kinetics and electrical properties of Pb(Zr_{0.9}Ti_{0.1})O₃ doped with Cerium oxide’
- [103] Bondzie VA, Kleban P and Dwyer DJ, XPS identification of the chemical state of subsurface oxygen in the O/Pd(110) system, *Surf. Sci.* 347, 319-328 (1996)
- [104] DiDio RA, Zehner DM and Plummer EW, An angle-resolved UPS study of the oxygen-induced reconstruction of Cu(110), *J Vac Sci Technol A2*, 852-855 (1984).
- [105] Warren S, Flavell W R, Thomas A G, Hollingworth J, Wincott P L, Prime A F, Downes S and Chen C, Photoemission studies of single crystal CuO(100), *J Phys Condens Matter* 11, 5021-5043 (1999).
- [106] Pforte F, Gerlach A, Goldmann A, Matzdorf R, Braun J, and Postnikov A, Wave-vector-dependent symmetry analysis of a photoemission matrix element: The quasi-one-dimensional model system Cu(110)(2×1)O’ *Phys Rev B* 63, 165405 (2001).
- [107] Dose V, Momentum-resolved inverse photoemission, *Surf Sci Rep* 5, 337-378 (1986).
- [108] Spitzer A and Luth H, The adsorption of oxygen on copper surface: I Cu(100) and Cu(110), *Surf Sci* 118, 121-135 (1982); The adsorption of oxygen on copper surface: II Cu(111), *Surf Sci* 118, 136-144 (1982).
- [109] Sekiba D, Ogarane D, Tawara S, Yagi-Watanabe K, Electronic structure of the Cu-O/Ag(110)(2×2)p2mg surface, *Phys Rev B* 67, 035411 (2003).
- [110] Alfe D, de Gironcoli S, Baroni S, The reconstruction of Rh(100) upon oxygen adsorption, *Surf Sci* 410, 151-157 (1998).
- [111] Bondzie VA, Kleban P and Dwyer DJ, XPS identification of the chemical state of subsurface oxygen in the O/Pd(110) system, *Surf Sci* 347, 319-328 (1996).
- [112] Zhang J, Dowben PA, Li D, Onellion M, Angle-resolved photoemission study of oxygen chemisorption on Gd(0001), *Surf Sci* 329, 177-183 (1995).
- [113] Böttcher A and Niehus H, Oxygen adsorption on oxidized Ru(0001), *Phys Rev B* 60(20), 14396-14404 (1999).
- [114] Böttcher A, Conrad H, Niehus H, Reactivity of oxygen phases created by the high temperature oxidation of Ru(0001), *Surf Sci* 452, 125–132 (2000).
- [115] Bester G, and Fähnle M, On the electronic structure of the pure and oxygen covered Ru(0001) surface, *Surf Sci* 497, 305-310 (2002).
- [116] Stampfl C, Ganduglia-Pirovano MV, Reuter K, and Scheffler M, Catalysis and corrosion: The theoretical Surface-science context, *Surf Sci* 500, 368-394 (2002).
- [117] Schwegmann S, Seitsonen AP, De Renzi V, Dietrich D, Bludau H, Gierer M, Over H, Jacobi K, Scheffler M, and Ertl G, Oxygen adsorption on the Ru(100) surface, Anomalous coverage dependence, *Phys Rev B* 57, 15487-15495 (1998).
- [118] Mamy R, Spectroscopic study of the surface oxidation of a thin epitaxial Co layer, *Appl Surf Sci* 158, 353–356 (2000).
- [119] Zheng JC, Xie XN, Wee ATS and Loh KP, Oxygen induces surface states on diamond (100), *Diamond Rel Mater* 10, 500-505 (2001).
- [120] Tibbetts GG, Burkstrand JM, and Tracy JC, Electronic properties of adsorbed layers of nitrogen, oxygen, and sulfur on copper (100), *Phys Rev B* 15, 3652-3660 (1977).
- [121] Tibbetts GG and Burkstrand JM, Electronic properties of adsorbed layers of nitrogen, oxygen, and sulfur on silver (111), *Phys Rev B* 16, 1536-1541 (1977).
- [122] He P and Jacobi K, Vibrational analysis of the 1×1-O overlayer on Ru(0001), *Phys Rev B* 55, 4751-4754 (1997).
- [123] Moritz T, Menzel D and Widdra W, Collective vibrational modes of the high-density (1×1)-O phase on Ru(001), *Surf Sci* 427-428, 64-68 (1999).

-
- [124] Frank M, Wolter K, Magg N, Heemeier M, Kühnemuth R, Bäumer M and Freund H-J, Phonons of clean and metal-modified oxide films, an infrared and HREELS study, *Surf Sci* 492, 270-284 (2001).
- [125] Sun CQ, Tay BK, Lau SP, Sun XW, Zeng XT, Bai HL, Liu H, Liu ZH, Jiang EY, Bond contraction and lone pair interaction at nitride surfaces *J Appl Phys* 90, L2615-2617 (2001).
- [126] Han WG and Zhang CT, A theory of non-linear stretch vibration of hydrogen bonds, *J Phys Condens Mat* 3, 27-35 (1991).
- [127] Pasquini L, Barla A, Chumakov AI, Leupold O, Ruffer R, Deriu A, and Bonetti E, Size and oxidation effects on the vibrational properties of amorphous Fe, *Phys Rev B* 66, 073410 (2002).